DEVELOPMENT OF A LONGITUDINAL RAIL STRESS MEASUREMENT DEVICE

A Thesis

by

SAMUEL JAMES HURLEY

Submitted to the Office of Graduate and Professional Studies of
Texas A&M University
in partial fulfillment of the requirements for the degree of

MASTER OF SCIENCE

Chair of Committee,   Stefan Hurlebaus
Committee Members,   Gary Fry
    Alan Palazzolo
Head of Department,   Robin Autenrieth

December 2014

Major Subject: Civil Engineering

ABSTRACT

The continuous welded rails used in most of the United States lack expansion joints of any sort. This leads to a much smoother ride and a longer service life for rails and wheels, but also causes extreme temperatures to induce high stresses in these rails. In very warm conditions these stresses can incite sudden buckling of the rails, which is dangerous and difficult to predict. To alleviate these risks rail stresses need to be regularly monitored, but current practices are slow and labor intensive. This research develops a non-contact prototype apparatus designed to quickly measure longitudinal stress in rails. The measurement is performed by generating a Rayleigh wave along the surface of the web of the rail and analyzing the polarization of the Rayleigh wave some distance further down the rail.

An evaluation of this measurement technique is performed on rails of varying age and surface condition in a lab environment. A set of guidelines is then established to ensure the successful recreation of these results in a field environment. From these guidelines, a 3D model is developed to aid in the construction process. Finally, a prototype is manufactured based on this design.

ACKNOWLEDGEMENTS

First I would like to extend a huge "thank you" to my committee chair, Dr. Hurlebaus, and also to my committee members, Dr. Fry and Dr. Palazzolo, for their guidance and support throughout the course of this research.

Thanks also go to my friends, colleagues, and the faculty and staff in the Civil Engineering Department for making my time at Texas A&M University a worthwhile experience. I also want to extend my gratitude to the Transportation Technology Center Inc. for their interest and support in this research.

Finally, I would like to thank my family, who made all of this possible for me. To my mom and dad for providing great role models for my life, and to my wife for her constant motivation and love.

TABLE OF CONTENTS

LIST OF FIGURES

LIST OF TABLES

1. INTRODUCTION

The practice of installing continuous welded rail (CWR) has been used in the United States since the early 1930s, sparked by the discovery of the process of thermite welding (Lonsdale, 1999). The long rail members produced give CWR the advantage of a much smoother ride compared to previous methods of rail installation. The smoother ride, in turn, decreases abrasion between the rail and the wheels, which increases the service life of both. While using CWR has been widely beneficial, it comes with its own set of problems. The exceptionally long members react to thermal expansion or contraction as members with fixed ends, causing compressive stress in warmer temperatures, tensile stress in colder temperatures.

1.1 Background

Thermal rail buckling is a critical issue in modern railroads. Thermal effects on rails can cause high longitudinal forces in extreme temperatures. For a newly and properly installed rail, these extreme temperatures are often well beyond the normal range of temperatures experienced; however as tracks shift during service usage, these temperatures can become a reality. Sometimes, these thermal loads alone can induce a static buckling (Figure 1.1), but more often thermal buckling is precipitated by a vehicle load on the rail (Figure 1.1) (Kish et al., 2013).

These so-called "sun kinks" are dangerous as well as costly. According to Phillips (2012), more than 6000 derailments costing a combined total of over $1 billion in the past

Figure 1.1: Lateral track buckling (Kish et al., 2013).

decade were caused by internal defects and sun kinks. Figure 1.2 shows one recent

example of a lethal derailment that could have been prevented by monitoring thermal rail

stresses. The Union Pacific accident occurred near Chicago on July 4th, 2012. At the end

of a string of days with temperatures in the triple digits, a Union Pacific train carrying coal

derailed while crossing an 86-foot-long bridge over Shermer Avenue in Glenview, near

Figure 1.2: Chicago train derailment (Sadovi and Danna, 2012).

Chicago. Out of the 138 total rail cars, 31 derailed and piled up on the bridge, overloading it and causing it to collapse. The next day, while the rubble was being cleared away, a vehicle with two deceased passengers was discovered underneath. After further investigation, Union Pacific attributed the derailment to a sun kink caused by the extreme heat (Sadovi and Danna, 2012). This derailment could have been avoided if there was a more convenient method to measure the stress in rails.

The rail neutral temperature (RNT) is the temperature for which a rail experiences no stress, and is initially determined by the ambient temperature at the time of installation. In cases of extreme difference between the RNT and the ambient temperature, buckling or fracture may occur. A rail properly installed between high and low temperature

extremes for the area will decrease these dangers, but even a perfectly installed rail is not immune to thermal buckling or fracture. According to Kish and Samavedam (2005), a typical CWR track has a buckling force that corresponds to a temperature difference of 60 to 80^0F. For a rail with the common RNT of 90^0F, a buckling temperature of 150 to 170^0F is well above expected temperatures for normal operation. However, the RNT can change over time based on a variety of factors including typical rail maintenance, longitudinal rail movement, and vertical track settlement. Kish and Samavedam (2005) indicate that these shifts could change the RNT by as much as 40^0F, which would decrease the buckling temperature to around 110^0F—a rail temperature often achieved in the heat of the summer. For rails already heated from high ambient temperatures, thermal buckling can often be triggered by the trains passing over them, making them even more dangerous (Hirao et al., 1994). For these reasons, it is important to monitor the stress in CWR in order to determine rails that pose a high susceptibility to buckling.

Methods of measuring the stress in rails do exist and are currently in use; however, the most commonly used techniques are both labor intensive and time consuming, and as such they are insufficient for comprehensive monitoring demands.

1.2 Research Objective

The dangers of excessive rail stress are high, but there are simply too many miles of track to adequately monitor with today's time- and labor-intensive methods. With the development of an accurate and robust scannable rail stress measurement device, rails can be monitored much more frequently. As information on the stresses in rails increases, derailments caused by sun kinks will decrease. Furthermore, as the accumulated data of

4

rail stresses increases nationwide, new methods of preventing stress buildup can be more easily developed.

While there has been extensive research done on the various methods for measuring longitudinal rail stress, including the strengths and weaknesses of each, little research has gone into the final step of moving from theory to application and pushing these ideas into the field.

The first objective of this research is to further test the method of measuring the longitudinal stress in rails using Rayleigh wave polarization. This technique has proven effective in a controlled laboratory environment, however it will need to be proven as a robust method before finding any success in the field. To this end, the technique will be applied to a number of rails with varying surface conditions from different manufactures.

The second objective of this research is to provide an apparatus to simplify the measurement process. Initially this device will be developed as a stop-and-go measurement device, however future work could upgrade the apparatus to a fully mobile stress measurement system. The method of measuring stress will be developed so that the same technique can be used to determine the condition of the rail at the time of installation, and then monitored at any time during the lifespan of the rail.

1.3 Organization of Thesis

This thesis is divided into six chapters. The first chapter provides an introduction into the background and objectives of this research. Chapter 2 presents previous research performed on stress measurement techniques. Chapter 3 reviews the fundamentals of linear elasticity and wave propagation as needed to explain the polarization of Rayleigh

waves, and then covers nonlinear elasticity to explain the relationship between Rayleigh wave polarization and applied stress. Chapter 4 details the setup and procedure for measuring the polarization of Rayleigh waves in the lab, and also discloses the experimental results. The process of the prototype development and construction are reported in Chapter 5, and Chapter 6 discusses the conclusions and areas for future work.

2. LITERATURE REVIEW

According to Kish et al. (2013), standard methods of monitoring longitudinal rail forces make use of strain gages that are installed on rails determined to be at a high risk of buckling. While effective, these methods require a calibration of the strain gages with zero force in the rail, which is difficult and time consuming at any point after rail installation. Typically this calibration is accomplished by unclipping and cutting the rail to relieve longitudinal stress, installing strain gages, and then re-welding the rail. While effective in rails that must be cut as a part of rail maintenance (including destressing high-risk rails), cutting the rails for the sole purpose of calibrating strain gages is not ideal, as it is both destructive and labor intensive. Over the years, many alternatives have been proposed that attempt to solve these problems, but none has proven effective enough to replace this well-established method.

2.1 Rail Stress Measurement Techniques

As an alternative strain gage calibration technique, Kish and Samavedam developed the Rail Uplift Technique (Kish et al., 2013), which allows for absolute force calibration of strain gages without cutting the rail. This is accomplished by unclipping the rail and applying a vertical force through the use of a modified rail car (shown in Figure 2.1). The Rail Uplift Device (RUD) lifts the unclipped rail while pinning the rail at two points with its inner wheels, causing the enclosed section of rail to behave like a beam-column whose vertical deflection will depend on the known uplift force and the unknown
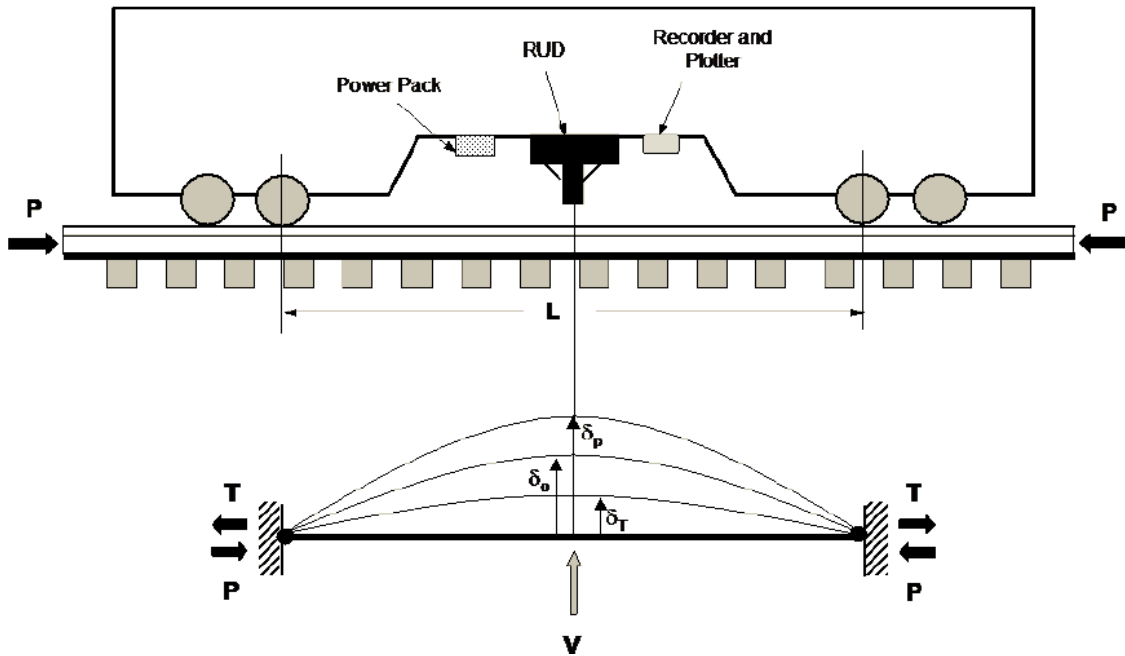
Figure 2.1: Rail Uplift Device schematic and principle (Kish et al., 2013).

longitudinal force. By measuring the deflection under a fixed uplift load (or the uplift load required for a fixed vertical deflection), the longitudinal force for a given section of rail can be determined, thereby allowing strain gage calibration without rail cutting.

To verify the efficacy of this method, tests were performed at TTCI in Pueblo, Colorado on tangent and 5-degree curved tracks. The team modified the RNT of their specimens by destressing at higher ambient temperatures to produce tensile loads, and by artificial rail heating to produce compressive loads. In both cases the test data was in good agreement with the theory. Following these results, the Rail Uplift Technique was used in the field to map several thousand feet of BNSF railroads. This analysis found a significant amount of variation in neutral temperatures, as seen in Figure 2.2; in particular, the second

8
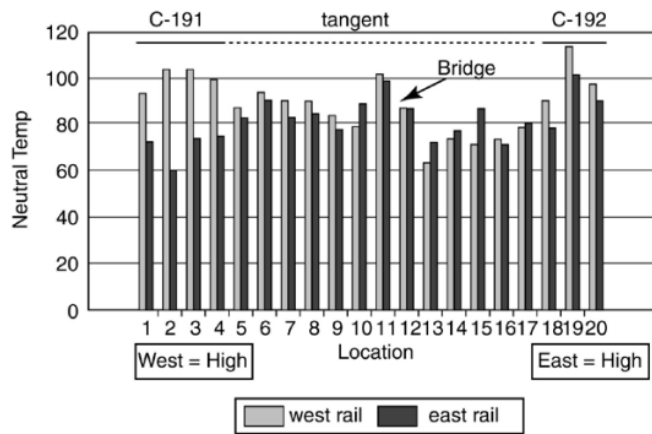
Neutral Temperature for Section 2
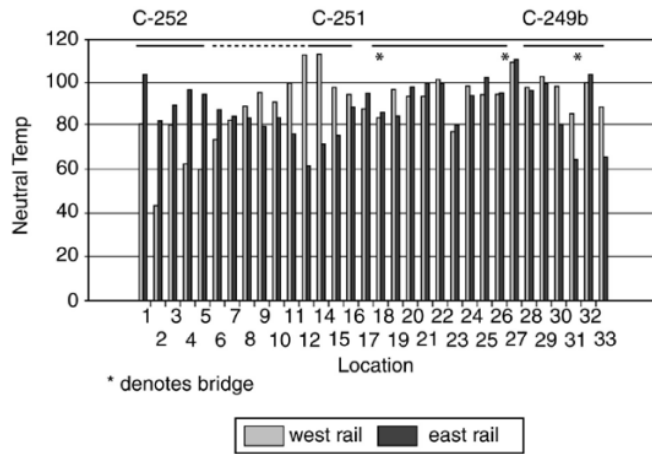
Neutral Temperature Variation for Section 3

Figure 2.2: Examples of neutral temperature measurements using the Rail Uplift Device (locations spaced 300 to 500 ft apart) (Kish et al., 2013).

plot shows that the RNT in two adjacent sections differs by nearly 60 degrees in curve C-252. Unfortunately complications in the method, such as having to remove the rail fasteners for the length of the specimen, has kept this method from gaining acceptance in the railroad industry (Kish et al., 2013).

9

The VERSE method, as described by Tunna (2000), also uses an uplift technique to measure the longitudinal loads in rails. However, instead of pinning either end of the unclipped length of rail, supports are placed between the rail and the crossties to provide a pinned end connection. A highly mobile jack frame, shown in Figure 2.3, is then affixed to the rail midway between the added supports. It then exerts an uplift load of 10 kN while the load and displacement is tracked by transducers and relayed to a handheld computer that can then calculate the RNT. Unfortunately, this method also suffers from limitations similar to the Rail Uplift Technique: unclipping the rail to make discrete measurements is costly and time-consuming.

Another non-destructive technique was explored by Damljanovic and Weaver in 2005. Rather than applying a static, vertical load, they proposed applying a lateral vibration and using that excitation to determine the lateral bending wave number of the

Figure 2.3: VERSE measurement system (VERSE, 2012).

specimen. Operating in the range of 200 Hz, they were able to produce promising results in a laboratory environment. In practice, however, this is a delicate measument that requires a high level of precision and accuracy in order to extract accurate measurements.

A similar technique is explored by Phillips (2012). In this experiment, Electro Mechanical Impedance (EMI) behavior is used to determine the stress in heated rails. In the method of EMI a small piezoelectric wafer is bonded to the neutral axis of the member being measured. Since the wafer is small and lightweight (typically ~½ in. across and less than 0.03 in. thick) it has no effect on the dynamic behavior of the member. When excited, the piezoelectric wafer will expand laterally, which exerts an axial force and a bending moment on the member. If the piezoelectric wafer is then excited at a specific frequency, these excitations will cause the member to oscillate at that frequency. By exciting the wafer over a range of frequencies, the resonance frequencies of the member can be found by observing the impedance of the piezoelectric element. When the internal stress of a member changes, commonly caused by heating or cooling of the member, the resonance frequencies will similarly change. Phillips (2012) performed this method for both fixed-fixed rails and free-free rails in order to determine what thermal effects of EMI are stress-independent. For the fixed-fixed rail experiment, two 70-ft. rails were installed and a pair of concrete blocks was poured around them at each end. The rails were then heated (with a maximum temperature of ~200 °F) and the resonance frequencies for the various temperatures were recorded. The free-free rail experiment was similar, except that the concrete blocks were absent and rollers were placed underneath the rails. The two setups

had nearly identical results, which shows that the stress-independent thermal effects on the resonant frequencies were dominating the measurement.

One update to the traditional method for determining internal stress is discussed by Ghita et al. (2010). This technique, rather than cutting an entire segment of the rail, involves drilling a small, shallow hole (typically 6mm across and 9mm deep), and applying a system of 3 strain gages around the opening. The rosette strain gage then measures the deformations around the hole, and the data is used to determine the stress. The method uses the same principles as the traditional method, but is considered to be only half-destructive because the bending capacity of the rail is not significantly altered (Ghita et al. 2010). One drawback of this technique is that holes must be drilled in multiple locations of the profile (head, web, etc.) in order to get an adequate reading. Furthermore, drilling the holes and applying the rosette strain gage cannot be automated easily and requires the track to be closed for the duration of the inspection. While this technique shows marked improvements over traditional methods in accuracy, with the added benefit of being minimally invasive, it is still labor intensive, and the necessary track closures are costly.

One stress measurement system that uses the magnetic properties of steel is applied to rails by Hayes (2008). The MAPS system, shown in Figure 2.4, was originally developed in the 1990's to non-destructively provide residual stress profiles of offshore jacket structures. The MAPS system doesn't distinguish between residual and applied stresses, and therefore requires a measurement of the sample free of applied stress. In rails,

this is accomplished by measuring the transverse residual stress and relating them to the longitudinal residual stress, since thermal loading in the transverse direction is negligible. Since all methods discussed so far are contact measurements, they must be performed at discrete intervals along the rail. Discrete measurements can be time consuming and cost intensive—requiring the technician to stop and measure the stress at points along the rail.
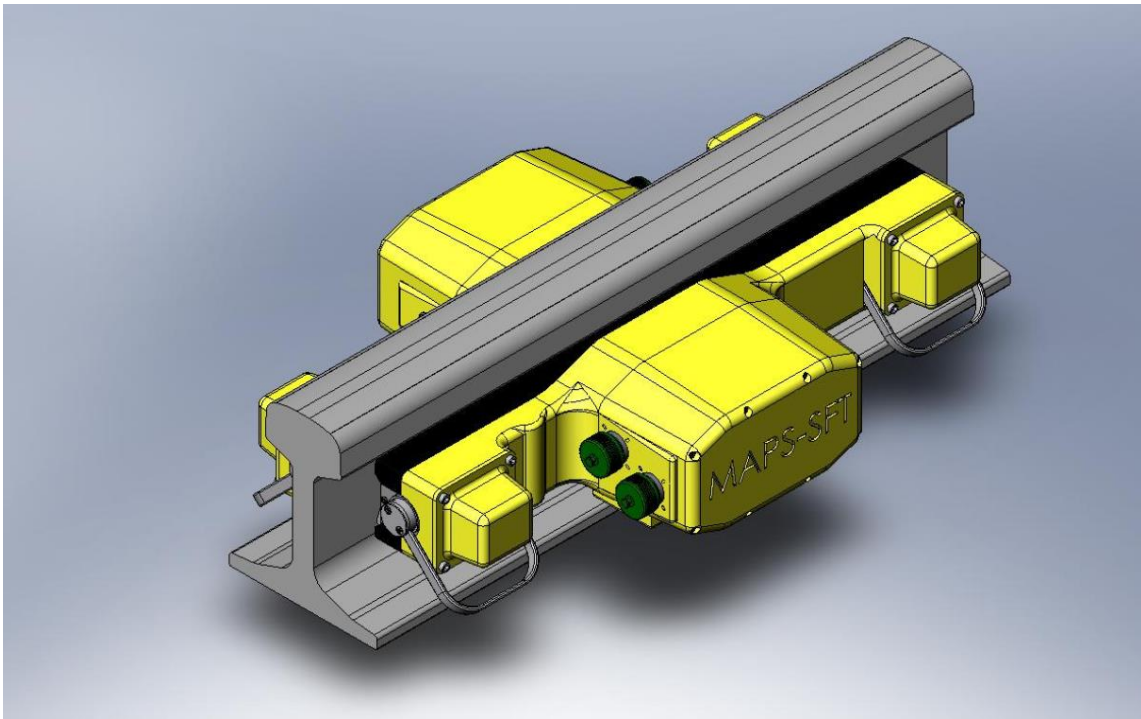
Figure 2.4: MAPS-SFT HUs shown attached to a section of 113A rail (Hayes, 2008).

An ideal stress-measurement device should be portable enough to be used in a rail vehicle or railroad car driven down the track at standard speeds. In order for this ideal to be realized, noncontact methods of measuring the stress must be utilized. Hirao et al.

(1994) mention that there are only two suitable contenders that meet the criteria: magnetic properties and ultrasonic waves.

2.2 Ultrasonic Stress Measurement

Nonlinearity in the stress-permeability relation makes measurement using magnetic properties very difficult, so the research performed by Hirao et al. (1994) was focused on ultrasonic waves. Through the use of electromagnetic-acoustic transducers, both excitations and measurements can be made without coming in direct contact with the rail. Hirao et al. (1994) explore two methods of utilizing ultrasonic frequencies to measure the birefringent acoustoelasticity and thereby the rail stress. Acoustoelastic birefringence is most easily understood as the difference in wave speed of two perpendicular shear waves propagating in the same direction. The first of the two methods involves high voltage bursts from the transducer that sweep through a range of frequencies to determine the frequencies which create resonance within the web of the rail. As the stress in the web increases, the resonance frequency also increases. The other method investigated detected phase shifts. In order to increase sensitivity, a large round-trip echo path is desirable. For this reason, this method makes use of the longest echo path in the cross section of the rail, from the top of the head to the bottom of the rail. The primary advantage of the phase shift detection approach is the very low measurement time (< 0.1 s), however it is not as robust a method as the resonance method. Since the phase shift method includes a measurement of the head, additional complications arise, including the top of the head not always being parallel to the bottom of the rail. While the resonance method takes longer to perform (10-

20s), the results are much more robust due to the number of overlapping reflection echoes (Hirao et al., 1994).

In the field of ultrasonic stress measurement, one of the earliest devices was developed by Egle and Bray (1979). This contact measurement method attached a series of transducers to the web of the rail which used the time of flight of longitudinal waves to determine changes in stress along the rail surface. In both laboratory and field tests they were able to determine changes in stress with an accuracy of ±1 ksi. A few years later, Bray and Leon-Salamanca (1985) released a paper that explored using head waves (longitudinal waves refracted at their first critical angle) rather than surface longitudinal waves. This method still uses time of flight, but finds bulk stress rather than surface stress. Furthermore, this method involves averaging discrete measurements along the specimen in order to minimize the effects of surface texture and residual stress. Bray (2002) later used the same technique to measure wall and weld stresses in a pressure vessel. Again, Bray took a series of measurements around the vessel to account for surface inconsistencies, and was able to produce data in close agreement with subsequent destructive tests.

As an alternative to longitudinal waves, Rayleigh waves have been shown to be an ideal excitation mechanism to measure surface stress. According to Husson et al. (1982), Rayleigh waves are most useful "real structural samples" where surface condition and member thickness are unknown, and when bulk stress can be inferred from surface stress. In their experiment, an edge-bonded transducer generated a Rayleigh wave and is detected by two electromagnetic transducers (EMATS). The EMATS are not in direct contact with

the surface, which reduces the effects of surface condition at the cost of decreased efficiency. The variation of the wave velocity measured by each of the EMATS is used to calculate the surface stress for a given acoustoelastic coefficient. Husson et al. (1982) verified this method on aluminum and 304 stainless steel, producing results that were in close agreement to outside experimental results.

Duquennoy et al. (1999) also used Rayleigh wave speed to determine stress. Using a pair of wedge transducers, they developed the apparatus shown in Figure 2.5. They then used this device to generate a strain profile for a laminated aluminum alloy specimen, which produced reasonable and repeatable results.
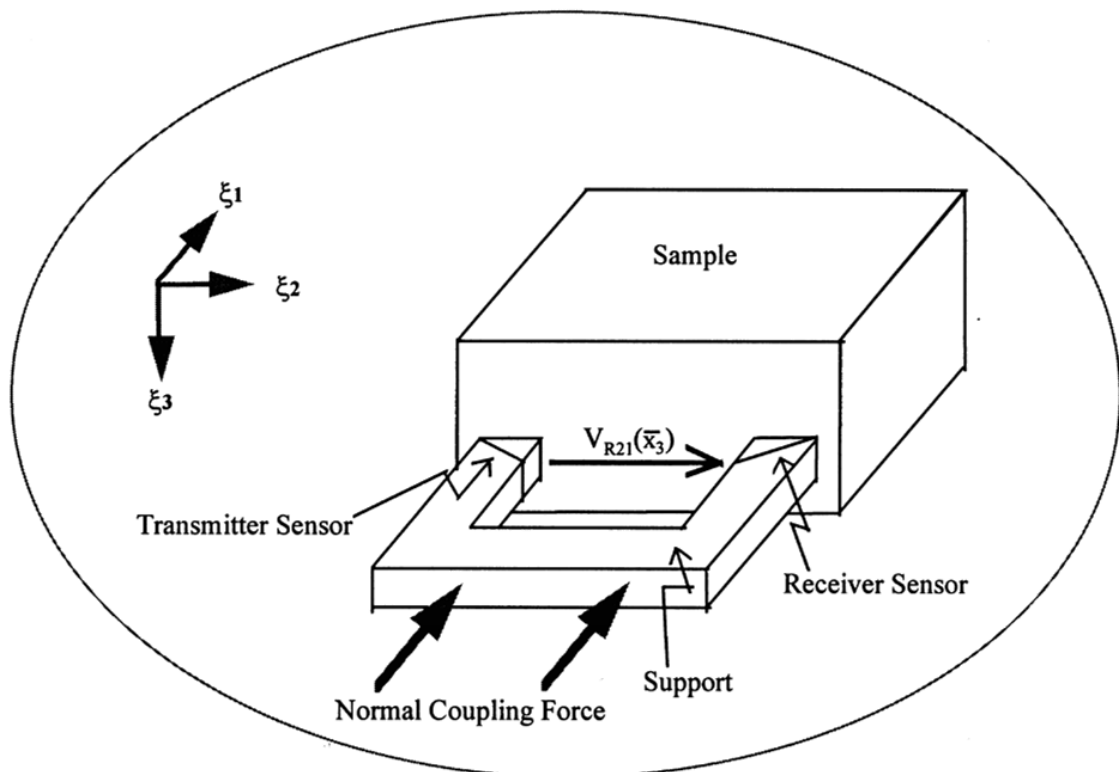
Figure 2.5: Rayleigh wave speed stress measurement device (Duquennoy et al., 1999).

This research will measure the polarization (rather than wave speed) of Rayleigh waves, as demonstrated by Djayaputra (2010). Djayaputra used a wedge transducer to generate Rayleigh waves along the web of the rail, then measured the in-plane and out-of-plane velocities using a laser Doppler vibrometer, and finally calculated the polarization of the Rayleigh wave from the phase shift of the in- and out-of-plane components, as shown in Figure 2.6. The advantages of this system of measurement are that high-frequency Rayleigh waves are non-integral (that is, they do not accumulate material properties along the wave propagation path) and that the polarization of Rayleigh wave is an order of magnitude more sensitive than the Rayleigh wave speed (Djayaputra, 2010).
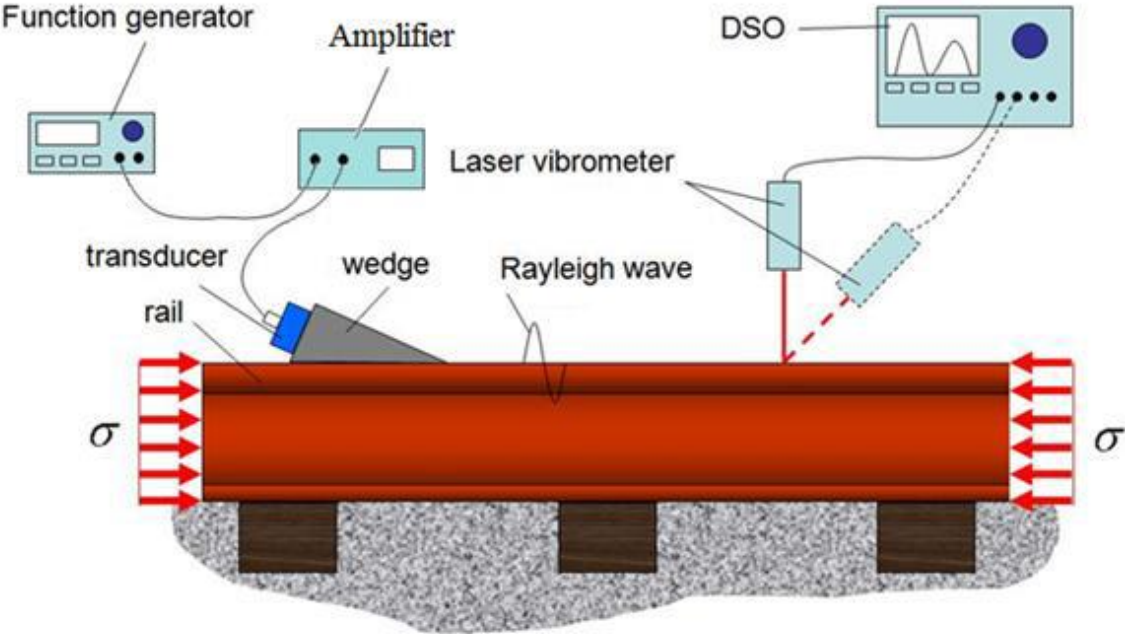
Figure 2.6: Measuring rail stress using Rayleigh waves (Djayaputra, 2010).

3. THEORETICAL BACKGROUND

In order to better understand the stresses and wave propagation in a solid body, the following sections review the fundamental equations of motion for a linear elastic continuum. Then, to fully observe the relationship between the two, an overview of nonlinear elasticity is provided.

3.1 Linear Elasticity

For any arbitrary continuous volume V, defined by the closed surface A, and located in a three-dimensional coordinate system with axes x_1, x_2, and x_3, consider the point P_0 and a neighboring point P_1 which are both within V. Initially, the location of P_0 is defined by the vector X_i, with P_1 located dX_i away from P_0. If a deformation is induced along the surface, V, A, P_0, and P_1 become V', A', P'_0, and P'_1 respectively, where the
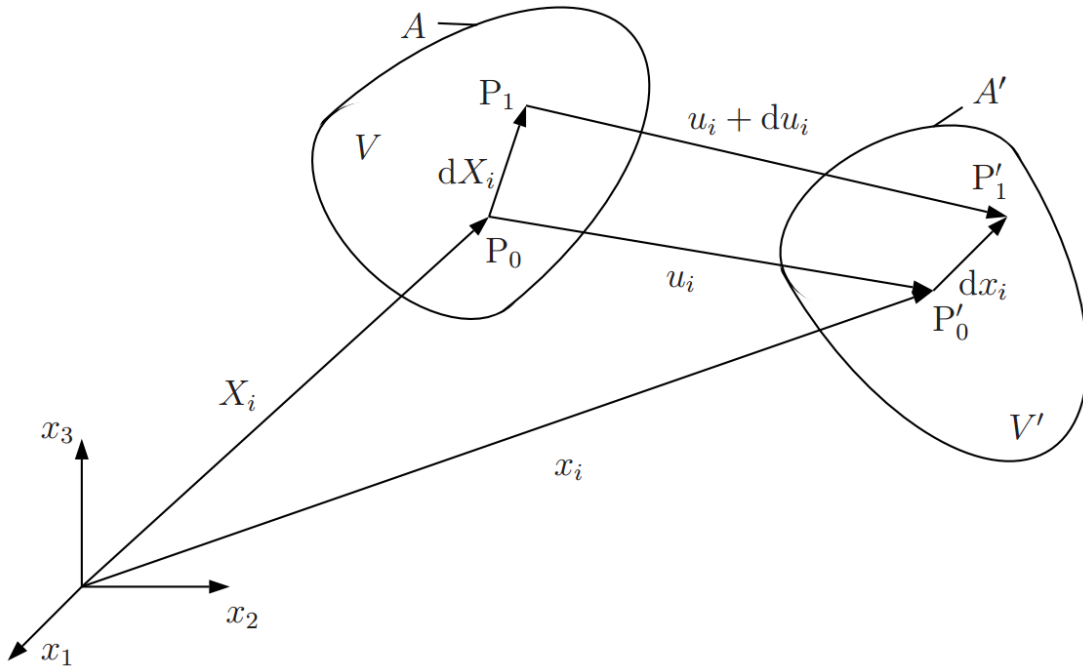
Figure 3.1: Deformation of a continuous medium (Hurlebaus, 2005).

18

location of P'_0 is now defined by the vector x_i, with P'_1 located dx_i away from P'_0. The

displacement of P_0 to P'_0 is defined by the vector u_i, and the displacement of P_1 to P'_1 is

similarly defined by the vector $u_i + du_i$, as shown in Figure 3.1.

Using the linearized theory of deformation and written with Einstein summation

notation, Hurlebaus (2005) relates the displacement at $x + dx$ to the displacement at x by

$$u_i(x + dx) = u_i(x) + u_{i,j}dx_j$$

(3.1)

where $u_{i,j}$ is assumed to be small ($\ll 1$). This leads to $du_i = u_{i,j}dx_j$, which describes the

change of a volume element. $u_{i,j}$ can be more precisely discussed by examining the

changes induced by a strain component and by a rotation component

$$u_{i,j} = \frac{1}{2}(u_{i,j} + u_{j,i}) + \frac{1}{2}(u_{i,j} - u_{j,i})$$

(3.2)

$$u_{i,j} = \varepsilon_{ij} + \Omega_{ij}$$

(3.3)

where ε_{ij} is the symmetric small strain tensor and Ω_{ij} is the antisymmetric rotation tensor.

Another fundamental piece in the interplay between wave propagation and stress

is the Cauchy stress tensor. Any arbitrary surface force, dF, acting over the infinitesimal

plane dA can be modeled as a traction force, t, acting at a point

$$t = \frac{dF}{dA} \ .$$

(3.4)

This traction force can in turn be expressed by components perpendicular and

parallel to dA known as the normal stress, σ, and the shear stress, τ, respectively. For any

infinitesimal cube within a volume in R3, there may be three such traction forces which

each have a normal stress and two shear stresses. This relationship is expressed with the Cauchy stress tensor by

$$t_i = n_j \sigma_{ji}$$

(3.5)

where n_j is the unit normal vector oriented along the jth axis.

The symmetry of the stress tensor can by proven using balance of angular momentum. Hurlebaus (2005) states the balance of angular momentum as "the time rate of change of angular momentum is equal to the sum of the moments on the body." This can be expressed mathematically as

$$\frac{D}{Dt} \int_V \epsilon_{ijk} x_j v_k \rho \, dV = \int_A \epsilon_{ijk} x_j t_k \, dA + \int_V \epsilon_{ijk} x_j f_k \rho \, dV$$

(3.6)

where ϵ_{ijk} is the Levi-Civita symbol (not to be confused with the small strain tensor ε_{ij}), v_k is the material derivative of u_k, f_k is a body force acting on the entire volume, and ρ is the mass density of the volume. Reynold's transport theorem states

$$\frac{D}{Dt} \int_V \rho \, dV = \int_V \left(\frac{D\rho}{Dt} + \rho v_{i,i} \right) dV$$

(3.7)

which allows the left hand side of Equation (3.6) to be rewritten as

$$\int_V \left(\epsilon_{ijk} \frac{Dx_j}{Dt} v_k \rho + \epsilon_{ijk} x_j \frac{Dv_k}{Dt} \rho + \epsilon_{ijk} x_j v_k \frac{D\rho}{Dt} + \epsilon_{ijk} x_j v_k \rho \dot{x}_{k,k} \right) dV \ .$$

(3.8)

Since $\frac{Dx_j}{Dt} = v_j$, and $\epsilon_{ijk} v_j v_k = v \times v$, the first term of Equation (3.8) goes to zero.

Likewise, the last two terms can be shown to equal to zero by enforcing conservation of mass. For a continuous volume with no mass sources or sinks, the total mass does not change with respect to time

20

$$\frac{D}{Dt}m = \frac{D}{Dt}\int_V \rho \, dV = 0 \ . \tag{3.9}$$

Again employing Reynold's transport theorem yields

$$\frac{D}{Dt}m = \int_V \left(\frac{D\rho}{Dt} + \rho v_{i,i}\right) dV = 0 \ , \tag{3.10}$$

and evaluating the integral gives the so-called continuity equation

$$\frac{D\rho}{Dt} + \rho v_{i,i} = 0 \ . \tag{3.11}$$

Now, by regrouping the last two terms of Equation (3.8)

$$\epsilon_{ijk}x_j v_k \frac{D\rho}{Dt} + \epsilon_{ijk}x_j v_k \rho \dot{x}_{k,k} = \epsilon_{ijk}x_j v_k \left(\frac{D\rho}{Dt} + \rho v_{i,i}\right) = 0 \ , \tag{3.12}$$

they can be seen to vanish. This leaves only the second term from Equation (3.8), which can be simplified if the material derivative is approximated as the partial time derivative by neglecting the convective term

$$v_i = \frac{\partial u_i}{\partial t} + \frac{\partial u_i}{\partial x_i}\dot{x}_i \approx \frac{\partial u_i}{\partial t} = \dot{u}_i \tag{3.13}$$

$$\frac{Dv_i}{Dt} \approx \ddot{u}_i \ . \tag{3.14}$$

This allows Equation (3.6) to be rewritten as

$$\int_V \epsilon_{ijk}x_j \ddot{u}_i \rho \, dV = \int_A \epsilon_{ijk}x_j t_k \, dA + \int_V \epsilon_{ijk}x_j f_k \rho \, dV \ . \tag{3.15}$$

The right hand side of Equation (3.15) can be simplified by invoking Gauss' divergence theorem, which relates surface integrals to volume integrals by

$$\int_A n_i u_i \, dA = \int_V u_{i,i} \, dV \ .$$

(3.16)

Using Equation (3.16) along with Equation (3.5) simplifies Equation (3.15) to

$$\int_V \epsilon_{ijk} x_j \ddot{u}_i \rho \, dV = \int_V \left(\epsilon_{ijk} x_j \sigma_{kl,l} + \epsilon_{ijk} \sigma_{jk} \right) dV + \int_V \epsilon_{ijk} x_j f_k \rho \, dV$$

(3.17)

$$\int_V \epsilon_{ijk} \sigma_{jk} \, dV + \int_V \epsilon_{ijk} x_j \left(\sigma_{kl,l} + f_k \rho - \ddot{u}_i \rho \right) dV = 0 \ .$$

(3.18)

The term $\sigma_{kl,l} + f_k \rho - \ddot{u}_i \rho$ can be shown to go to zero by exploring conservation of linear momentum. Linear momentum is expressed as

$$\frac{D}{Dt} \int_V v_i \rho \, dV = \int_A t_i \, dA + \int_V f_i \rho \, dV \ .$$

(3.19)

Applying Equations (3.16) and (3.5) to the first term of the right hand side of Equation (3.19) allows conservation of momentum to be restated as

$$\frac{D}{Dt} \int_V v_i \rho \, dV = \int_V \sigma_{ji,j} \, dV + \int_V f_i \rho \, dV$$

(3.20)

$$\int_V \left(\sigma_{ji,j} + f_i \rho - \frac{Dv_i}{Dt} \rho \right) dV = 0 \ .$$

(3.21)

By applying Equation (3.13) and assuming no discontinuities within the volume,

$$\sigma_{ji,j} + f_i \rho - \ddot{u}_i \rho = 0 \ .$$

(3.22)

Zeroing out the second term of Equation (3.17) and assuming a continuous integrand yields

$$\epsilon_{ijk} \sigma_{jk} = 0$$

(3.23)

22

$$\sigma_{ij} = \sigma_{ji} \; .$$

(3.24)

The small strain tensor and Cauchy's stress tensor are related to each other by

$$\sigma_{ij} = E_{ijkl}\varepsilon_{kl} \; ,$$

(3.25)

which is known as the generalized Hooke's law for a linear elastic material. The symmetry of the stress and small strain tensors allows the fourth order stiffness tensor, E_{ijkl}, to be expressed by a 6-by-6 matrix of 21 constants for anisotropic materials. For isotropic materials, the stress-strain relationship is even further simplified to depend on only the two constants μ and λ, known as Lamé's constants

$$\sigma_{ij} = 2\mu\varepsilon_{ij} + \lambda\delta_{ij}\varepsilon_{kk} \; ,$$

(3.26)

where δ_{ij} is the Kronecker delta. Hurlebaus (2005) relates Lamé's constants to Young's modulus, E, the shear modulus, G, and Poission's ratio, ν, by

$$\mu = G = \frac{E}{2(1+\nu)} \quad \text{and} \quad \lambda = \frac{E\nu}{(1+\nu)(1-2\nu)} \; .$$

(3.27)

3.1.1 Wave Propagation

Wave propagation behavior in a homogeneous, isotropic, linear elastic material is governed by the equations of motion found in Equation (3.22). Applying the symmetry simplifications and expressing the stress in terms of derivatives of u_i and Lamé's constants allows the equations of motion to be rewritten as the Lamé-Navier equations

$$(\lambda + \mu)u_{i,ij} + \mu u_{j,ii} + \rho f_j = \rho \ddot{u}_j \; .$$

(3.28)

The Lamé-Navier equations can be solved for a system with no body forces ($\rho f_j = 0$) by employing the Helmholtz decomposition

23

$$u_i = \Phi_{,i} + \epsilon_{ijk}H_{k,j} \ .$$
(3.29)

Plugging this into Equation (3.28) and using the identity $\left(\Phi_{,j}\right)_{,ii} = \left(\Phi_{,ii}\right)_{,j}$ along with the additional constraint $H_{i,i} = 0$ allows Equation (3.28) to be grouped and rewritten as

$$\left\{(\lambda + 2\mu)\Phi_{,ii} - \rho\ddot{\Phi}\right\}_{,j} + \ \epsilon_{ijk}\left\{\mu H_{k,ii} - \rho\ddot{H}_k\right\}_{,j} = 0 \ .$$
(3.30)

This expression holds true if both terms in brackets are equal to zero so that

$$\frac{(\lambda + 2\mu)}{\rho}\Phi_{,ii} = \ddot{\Phi}$$
(3.31)

$$\frac{\mu}{\rho}H_{k,ii} = \ddot{H}_k$$
(3.32)

Equations (3.31) and (3.32) are both in the form of the wave equation, with wave speeds given by $c_L{}^2 = (\lambda + 2\mu)/\rho$ and $c_S{}^2 = \mu/\rho$, respectively. From the Helmholtz decomposition, it is know that Equation (3.31) represents an irrotational or curl-free wave, which is more commonly known as a longitudinal wave. Similarly, Equation (3.32) represents a solenoidal or divergence-free wave known as a shear wave. These two wave types are the only two that can exist in an infinite media (Graff, 1991), but wherever a boundary is introduced, a third type of wave can occur.

3.1.2 Rayleigh Waves

This third wave type is named after Lord Rayleigh, who was the first person known to have investigated them. According to Graff (1991), these types of waves were of interest to early seismologists who observed that earthquake events commonly involved two minor disturbances followed by a much stronger disturbance. The first two tremors were the shear and longitudinal waves whose lower energy is a result of the waves propagating

down into the earth as well as along the surface. By this logic, the slower and more powerful tremor would be caused by a wave that expends almost all of its energy propagating along the surface.

For such a wave propagating along the surface in the x_1-direction with wave speed c and wave number k, the solutions of Φ and H must be of the form

$$\Phi = F(x_3)e^{ik(x_1-ct)} \tag{3.33}$$

$$H_2 = G(x_3)e^{ik(x_1-ct)} \tag{3.34}$$

so that the wave can be shown to decay rapidly as it travels away from the surface in the x_3-direction. Putting these expressions into Equations (3.31) and (3.32) reveals an exponential growth and an exponential decay function each for $F(x)$ and $G(x)$. Imposing the known decay of Rayleigh waves allows the solutions corresponding to growth to be discarded leaving

$$\Phi = Ae^{-x_3\sqrt{k^2-k_L^2}}e^{ik(x_1-ct)} \tag{3.35}$$

$$H_2 = Be^{-x_3\sqrt{k^2-k_S^2}}e^{ik(x_1-ct)} \tag{3.36}$$

where k_L and k_S are the wave number of the corresponding longitudinal and shear waves. In order to find a solution for A and B, the boundary condition $\sigma_{13}(x_3 = 0) = \sigma_{33}(x_3 = 0) = 0$ is imposed, which leads Graff (1991) to the following equation for the wave speed

$$\left(2 - \frac{c^2}{c_S^2}\right)^2 = 4\sqrt{\left(1 - \frac{c^2}{c_L^2}\right)\left(1 - \frac{c^2}{c_S^2}\right)} \, , \tag{3.37}$$

where c_L and c_S are the longitudinal and shear wave speeds. It is worth noting that real roots for the right hand side of Equation (3.37) exist only for $c < c_S$ and $c < c_L$, which means that the Rayleigh wave is slower than both the shear and longitudinal waves, as expected. Furthermore, the Rayleigh wave speed is independent of wave number (and thereby wavelength) which makes it nondispersive. By recognizing Equation (3.37) as a reduced cubic equation in $(c/c_S)^2$, Graff (1991) states that roots of this cubic function depend only on Poisson's ratio, and Viktorov (1966) has shown that for all real media $(0 < v < 0.5)$, only one such root exists. Graff has approximated this relationship by

$$\frac{c}{c_S} = \frac{0.87 + 1.12v}{1 + v} \ . \tag{3.38}$$

Inserting Equations (3.35) and (3.36) with the solution for A and B into Equation (3.29) yields the following displacement expressions

$$u_1 = a(k) \ \sin\{k(x_1 - ct)\}$$
$$u_3 = b(k) \ \cos\{k(x_1 - ct)\} \ . \tag{3.39}$$

The equations above describe a particle with elliptical motion that is retrograde compared to the direction of wave propagation. This means that a wave travelling to the right will induce a counterclockwise motion in individual particles, as shown in Figure 3.2.

As shown earlier, the particle motion decreases rapidly with depth. Within a fairly shallow depth, 0.192λ according to Graff (1991), the retrograde motion reverses so that a wave propagating to the right will contain particles travelling counterclockwise at the surface and particles travelling clockwise just below the surface.
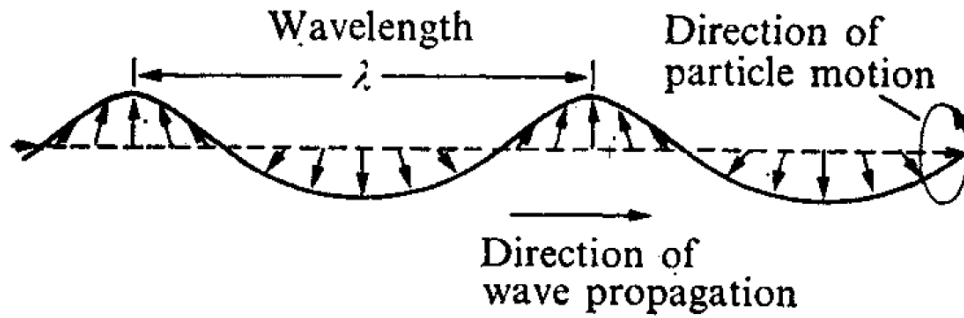
Figure 3.2: Rayleigh wave particle motion (Graff, 1991).

3.1.3 Polarization of Rayleigh Waves

The particle motion within a Rayleigh wave can also be described by its polarization, defined as the ratio of maximum in-plane displacement to maximum out-of-plane displacement of a particle on the surface

$$\Pi = \frac{\bar{u}_1}{\bar{u}_3} \tag{3.40}$$

For real media, Graff (1991) says that the out-of-plane displacement is always greater than the in-plane—typically 1.5 times greater, yielding a polarization value of around 0.67.

3.2 Nonlinear Elasticity

The linear elastic model developed above incorrectly indicates that wave propagation is independent of applied stress because it fails to account for variation in material properties with applied stress. In order to account for this relationship, the model must be expanded to include the previously neglected third-order elastic constants.

For the linear elastic model, the second-order elastic constants of an isotropic material depend only on Lame's constants and are given by

27

$$E_{ijkl} = \lambda \delta_{ij} \delta_{kl} + \mu \left(\delta_{ik} \delta_{jl} + \delta_{il} \delta_{jk} \right) .$$

(3.41)

To account for higher order effects, Junge (2003) gives the stiffness tensor by

$$E_{ijklmn} = v_1 \left(\delta_{ij} \delta_{kl} \delta_{mn} \right) + v_2 \{ \delta_{ij} (\delta_{km} \delta_{ln} + \delta_{kn} \delta_{lm}) + \delta_{kl} (\delta_{im} \delta_{jn} +$$

$$\delta_{jm} \delta_{in}) + \delta_{mn} (\delta_{ik} \delta_{jl} + \delta_{il} \delta_{jk}) \} + v_3 \{ \delta_{ik} (\delta_{jm} \delta_{ln} +$$

$$\delta_{jn} \delta_{lm}) + \delta_{jl} (\delta_{im} \delta_{kn} + \delta_{in} \delta_{mk}) + \delta_{il} (\delta_{jm} \delta_{kn} +$$

$$\delta_{jn} \delta_{mk}) + \delta_{jk} (\delta_{im} \delta_{ln} + \delta_{in} \delta_{lm}) \}$$

(3.42)

where v_1, v_2, and v_3 are the third-order elastic constants. The second-order, nonlinear constitutive stress strain relation is given by

$$\sigma_{ij} = E_{ijkl} \varepsilon_{kl} + \frac{1}{2} E_{ijklmn} \varepsilon_{kl} \varepsilon_{mn} ,$$

(3.43)

Another assumption of the previous derivation is that the initial position is assumed to be stress-free, which is often not the case in physical situations. For example, rail steel left out in the sun would likely have initial stress induced by the manufacturing process alongside stress imposed by static thermal loads. Therefore an additional body state is added to the two states shown in Figure 3.1, the natural state. The natural state is defined as a stress-free body, and the initial state is defined as a body with stress induced by static deformation from the natural state. This relationship is shown by Pao et al. (1984) in Figure 3.3. Since most material properties, including material density and Young's modulus, are defined with respect to a material's natural state, and since higher order elastic effects include changes in material properties with respect to stress, the stress of the initial state must be incorporated into the model.

For a body with homogenous initial stresses, the equations of motion are given by

$$\left(\delta_{ik}\sigma_{ij}^{i} + \hat{C}_{ijkl}\right)u_{k,jl} = \rho^{0}\left(1 - \varepsilon_{nn}^{i}\right)\ddot{u}_{i} \tag{3.44}$$

where σ^{i} and ε^{i} are the Cauchy stress and small strain tensors with respect to the initial

state, and ρ^{0} is the mass density of the natural state (Junge et al., 2006). $\hat{C}_{ijkl}$ is defined

by Pao et al. (1984) as

$$\hat{C}_{ijkl} = E_{ijkl}\left(1 - \varepsilon_{nn}^{i}\right) + E_{ijklmn}\varepsilon_{mn}^{i} + E_{mjkl}u_{i,m}^{i} + E_{imkl}u_{j,m}^{i}$$

$$+ E_{ijml}u_{k,m}^{i} + E_{ijkm}u_{l,m}^{i} \; . \tag{3.45}$$

Since mass density is affected by deformations, Equation (3.44) makes use of the fact that

the mass density in the initial state can be approximately related to the mass density in the

natural state by $\rho^{i} \approx \rho^{0}\left(1 - \varepsilon_{nn}^{i}\right)$.
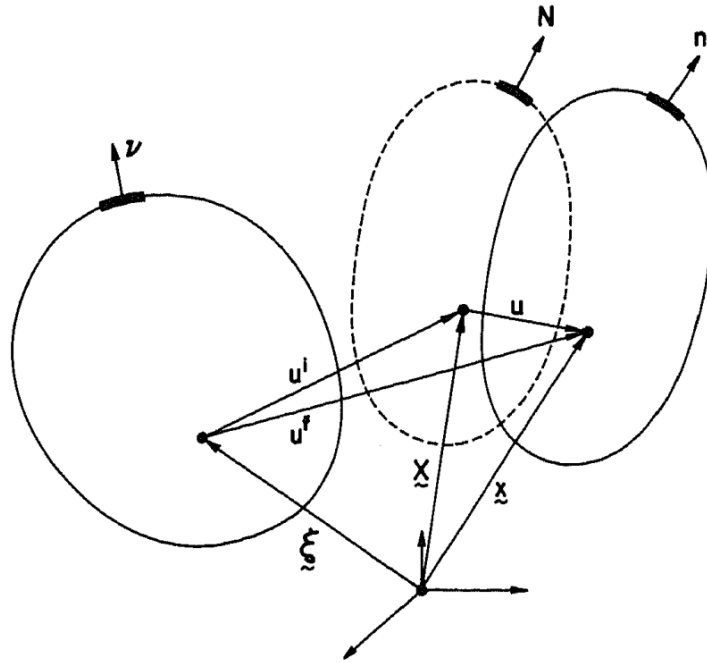
Figure 3.3: Coordinates for the three states of a pre-stressed body (Pao et al., 1984).

3.2.1 Wave Propagation

The solution to Equation (3.44) for a plane wave traveling in the x_1-direction is of the form

$$u_j = b_j P_{d_j} e^{ik(x_1 - ct)} \tag{3.46}$$

where b_j is the displacement field and P_d is the decay function. u_j can be related to its second time derivative as a simple harmonic oscillator by

$$\ddot{u}_j = -k^2 c^2 u_j = -\omega^2 u_j \ . \tag{3.47}$$

Additionally, through tensor analysis, Rose (2004) shows that

$$u_{k,jl} = k_j k_l u_k \ . \tag{3.48}$$

By applying these three relations to Equation (3.44), the equation of motion can be rewritten as

$$\left(\delta_{ik} \sigma_{ij}^i + \hat{C}_{ijkl} \right) k_j k_l u_k = \rho^0 \left(1 - \varepsilon_{nn}^i \right) \omega^2 u_j \tag{3.49}$$

This equation can be further simplified by making use of $u_j = \delta_{jk} u_k$ and introducing the Christoffel acoustic tensor, $\lambda_{jk} = \left(\delta_{jk} \sigma_{il}^i + \hat{C}_{ijkl} \right) k_i k_l$

$$\left\{ \lambda_{jk} - \rho^0 \left(1 - \varepsilon_{nn}^i \right) \omega^2 \delta_{jk} \right\} u_k = 0 \ . \tag{3.50}$$

This equation can be expressed in the form of the Christoffel equation

$$[A]\{b\} = 0 \ . \tag{3.51}$$

Non-trivial solutions of this homogeneous equation exists only if the coefficient matrix A has a rank deficiency, so that

$$\|A\| = 0 \ .$$

(3.52)

3.2.2 Rayleigh Waves

For a Rayleigh wave traveling along the half space where $x_3 \leq 0$, the decay function is known to be of the form

$$P_{d_j} = e^{ipkx_3}$$

(3.53)

where p is the decay parameter. This allows Equation (3.46) to be written as

$$u_j = b_j e^{ik(x_1 + px_3 - ct)} \ ,$$

(3.54)

which can be used with Equation (3.49) to obtain (Junge et al., 2006)

$$\{(\delta_{ik}\sigma_{33}^i + \hat{C}_{i3k3})p^2 + (\delta_{ik}\sigma_{13}^i + \hat{C}_{i1k3} + \delta_{ik}\sigma_{31}^i + \hat{C}_{i3k1})p$$

$$+ (\delta_{ik}\sigma_{11}^i + \hat{C}_{i1k1}) - \delta_{ik}\rho^0(1 - \varepsilon_{nn}^i)c_R^2\} u_{\mathrm{k}} = 0$$

(3.55)

For the case where the stress is uniaxial and coincident with the direction of propagation, this is expressed by the Christoffel equation in the following form

$$[A]\{b\} = \left[p^2\hat{S} + p(\hat{R} + \hat{R}^T) + \hat{Q} + p^2\hat{S} - \rho^0(1 - \varepsilon_{nn}^i)c_R^2 \, I\right]\{b\} = 0$$

(3.56)

where the matrices $\hat{S}$, $\hat{R}$, and $\hat{Q}$ are defined by

$$\hat{S} = \hat{C}_{i3k3} \ , \qquad \hat{R} = \hat{C}_{i1k3} \ , \qquad \hat{Q} = \delta_{ik}\sigma_{11}^i + \hat{C}_{i1k1} \ ,$$

(3.57)

and I is the identity matrix.

Taking the determinate of the coefficient matrix A to solve for p yields three pairs of complex conjugate roots that still depend on the Rayleigh wave speed, c_R. Using these

31

eigenvalues to solve for the null vector of A returns an expression for the displacements given by

$$u = BP_d f e^{ik(x_1 - ct)} \; , \qquad\qquad (3.58)$$

where B is the matrix of the eigenvectors $[b_1, b_2, b_3]$, $P_d = I e^{ip_i k x_3}$, and the vector f represents the factors of the linear combination which are determined by the boundary conditions.

Imposing the boundary conditions of an initially stress free surface, $\sigma_{i3}^i = 0$ at $x_3 = 0$, along with a stress free surface in the final state, $\hat{C}_{i3kl} u_{k,l} = 0$ at $x_3 = 0$ yields

$$\left[\hat{R}^T B + \hat{S} B P \right] \{f\} = [D]\{f\} = 0 \; , \qquad\qquad (3.59)$$

where $P = I p_i$.

Solving for the null-space of D yields a solution for f, and the value of c_R that satisfies both $\|A\| = 0$ and $\|D\| = 0$ is the Rayleigh wave speed of a uniaxially prestressed body.

3.2.3 Polarization of Rayleigh Waves

The displacement at the surface is given by

$$u = Bf e^{ik(x_1 - ct)} \; . \qquad\qquad (3.60)$$

Therefore, the polarization defined in Equation (3.40) is given by

$$\Pi = \frac{(Bf)_1}{(Bf)_3} \qquad\qquad (3.61)$$

32

4. EXPERIMENTAL PROGRAM

This chapter discusses the equipment, configuration, and methodology used to generate Rayleigh waves and measure their polarization in a lab environment. This setup is used as the basis for the design of a field measurement apparatus, with specific adaptations discussed in Chapter 5.

4.1 Experimental Setup

The process begins with an excitation signal whose frequency, amplitude, and number of bursts per cycle are specified by a function generator. This signal is magnified with an RF amplifier before being sent to a wedge transducer, which transfers the excitation signal to the rail. In-plane and out-of-plane vibrations are detected further down
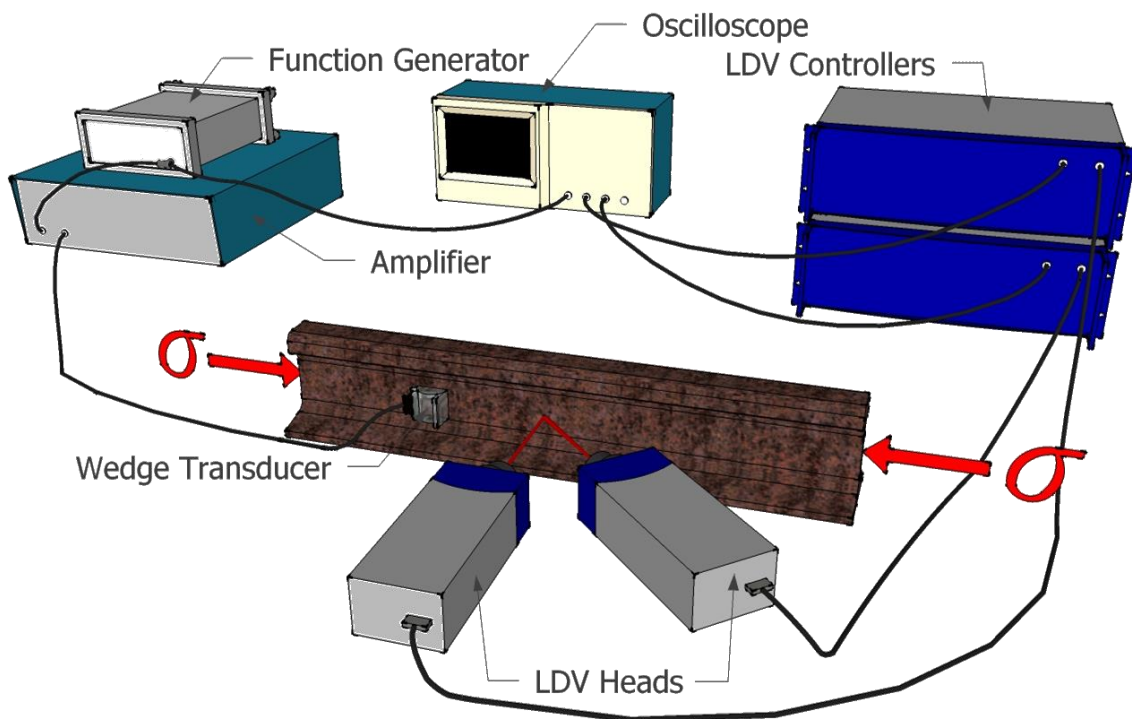
Figure 4.1: Experimental Rayleigh wave measurement setup.

the rail by a pair of laser Doppler vibrometers (LDVs), and then read by an oscilloscope. The data is transferred to a computer via Ethernet, and finally processed in Matlab to obtain the Rayleigh wave polarization. The setup is displayed in Figure 4.1. In order to simulate the stress of a CWR at a high temperature, a compressive load is applied to the rail segment using a hydraulic jack.

4.1.1 Function Generator and Amplifier

Signal generation is carried out using an Agilent 33250A function generator. The excitation signal is a 10 burst sine wave with a peak-to-peak amplitude of 1 V and frequency of 800 kHz. The amplifier is an E&I 2100L RF power amplifier with a 50 dB gain.

4.1.2 Transducer

The transducer used is a C401 Panametrics Angle Beam transducer with a center frequency of 1 MHz. The transducer is oriented with a 65° incidence angle by a Panametrics ABWX-2001 wedge. This angle is crucial to the generation of Rayleigh waves, as discussed in Section 4.2.

4.1.3 Laser Doppler Vibrometer (LDV)

The in- and out-of-plane vibration is detected by a pair of Polytec vibrometers. Each vibrometer is made up of an OFV-505 sensor head and an OFV-5000 modular controller. The LDVs operate on the principle of heterodyne laser interferometry, which is discussed by Hurlebaus (2005).

4.1.4 Data Acquisition and Signal Processing

The signal detected by the LDVs is recorded by a Tektronix TDS 3034C Digital Phosphor Oscilloscope (DPO). To maximize the signal-to-noise ratio, each reading is averaged over 512 cycles by the DPO. The averaged waveforms are then transferred to a networked computer using the DPO's web interface and analyzed using Matlab.

4.2 Rayleigh Wave Generation via Wedge Transducer

For any ultrasonic wave incident on a surface, a mode conversion will occur so that some of the energy may be transferred to the new material as longitudinal, shear, and surface waves while the rest will be reflected. The Rayleigh waves generated in this setup originate from ultrasonic longitudinal waves generated by a transducer that are incident at a specific angle. As stated earlier, this angle is critical because there exists an incident angle at which only Rayleigh waves will be generated. Figure 4.2 shows possible mode conversions for an incident longitudinal wave at angle θ_1 travelling from material 1 to material 2. The angle of the waves in material 2 is determined by the wave velocity, mathematically expressed using Snell's law

$$\frac{\sin \theta_1}{c_{L_1}} = \frac{\sin \theta_2}{c_{R_2}} = \frac{\sin \theta_3}{c_{L_2}} = \frac{\sin \theta_4}{c_{S_2}} \; . \tag{4.1}$$

For an incident angle that will generate a Rayleigh wave, $\theta_2 = 90° \Rightarrow \sin \theta_2 = 1$ so that

$$\sin \theta_1 = \frac{c_{L_1}}{c_{R_2}} \; . \tag{4.2}$$

Solving for the other two angles yields

$$\sin \theta_3 = \frac{c_{L_2}}{c_{R_2}} \quad \& \quad \sin \theta_4 = \frac{c_{S_2}}{c_{R_2}} \tag{4.3}$$
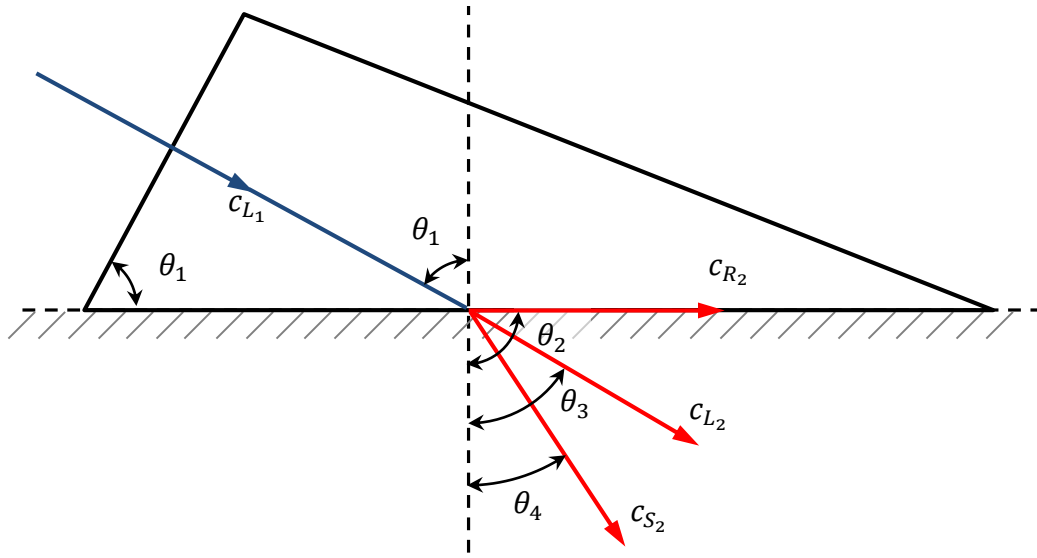
Figure 4.2: Mode conversion diagram.

The wedge has a known wave speed of 2720 m/s, and the Rayleigh wave speed for rail steel is typically assumed to be 3000 m/s (Djayaputra, 2010). With this information, the desired incident angle is found to be 65.0° using Equation (4.2). It can also be seen for a material like rail steel where $c_R < c_S < c_L$, that there is no angle that will satisfy either side of Equation (4.3). This means than neither longitudinal nor shear waves will be transmitted for this angle of incidence.

4.3 Experimental Procedure

For each measurement, the transducer was affixed to one side of the rail using a clamp and a fresh application of vacuum grease couplant to improve the signal strength. When placing the transducer, an effort was made to ensure it rested on a smooth surface of the rail, free of lettering or excessive rail degradation. Next, a compressive load of up to 40 T was slowly applied to the rail. The LDV's were then focused on a small spot and

36

aligned using translation stages. The surface velocity was acquired and averaged by the DPO, and then transferred to a computer for processing.

The data was analyzed by MATLAB to get the in-plane component using

$$\begin{Bmatrix} V_{IP} \\ V_{OP} \end{Bmatrix} = \frac{1}{\sin(\theta_a - \theta_b)} \begin{bmatrix} -\sin(\theta_b) & \sin(\theta_a) \\ \cos(\theta_b) & \cos(\theta_a) \end{bmatrix} \begin{Bmatrix} V_a \\ V_b \end{Bmatrix} \tag{4.4}$$

where V_{IP}, V_{OP} are the in-plane and out-of-plane particle velocities, respectively, θ_a, θ_b are the angles of the LDV relative to the web of the rail ($\theta_a = 90°$ and $\theta_b = 45°$ or $60°$), and V_a, V_b are the particle velocities measured under the angle of θ_a and θ_b, respectively. The particle displacements were then acquired by taking the integral of their respective velocity components. Finally, each of the peak in-plane displacements was divided by their corresponding out-of-plane displacements to obtain the Rayleigh wave polarization.

4.4 Experimental Results

Two experiments were performed on a variety of aged rails to explore the effects of a rail's manufacturing, age, and surface condition on the Rayleigh wave stress measurement. The first investigation, conducted at the Transportation Technology Center, Inc. (TTCI) facilities in Pueblo, CO, involved ten unstressed rail samples of varying age and surface condition. The second investigation was performed at Texas A&M's sensors lab and evaluated smaller segments of two of the same rails held under compressive loads.

4.4.1 Unstressed Rails

This experiment was performed on ten different rails provided by TTCI. The rails were chosen to represent a wide variety of rail manufactures and rail ages. Details about

the ten rail samples used are listed in Table 4.1, and profiles of each are shown in Figure

4.3.

Table 4.1: Branding and stamping of the TTCI rails.

Rail #	Branding (Raised Lettering)	Stamping (Depressed Letters)	Side	
			Field	Gage
1	136 RE NKK 1996 //////	346 S 120	Stamping	Branding
2	136 RE CF&I 1987 //////// METRA		Branding	Stamping
3	136 RE VT THYSSEN 1990 /////////	708136 HH	Branding	Stamping
4	HAYANGE 136 LBS RE 1981 //////	CSV 035 G 18	Branding	Stamping
5	141 AB HHC VT DO 2001 //////	3203R301	Stamping	Branding
6	136 RE VT JFE 2005 /	C6098 R III SP	Stamping	Branding
7	136 RE IH VT T2 2001 /	62244 R 303	Branding	Stamping
8	CORUS MS = 1060 E2	008298010	Stamping	Branding
9	136-10 CC BETH STEELTON 1993	275680 HH P65	Stamping	Branding
10	141 AB VT RMSM 2002-10	4 S DH 17	Branding	Stamping

For each side of each rail at least four sets of measurements were taken, and the

average of the polarization values was calculated. Table 4.2 and Figure 4.4 show the

Rayleigh wave polarization values for each rail. The results of the polarization

measurements show a relatively low coefficient variance between data points from a single

rail side, except for side G of the third rail. The third rail tested had a rough surface that

prevented the transducer from transmitting a strong signal.

The measured polarization values of each rail are similar and compare well with

the theoretical value of 0.66. This test shows that the proposed methodology is a promising

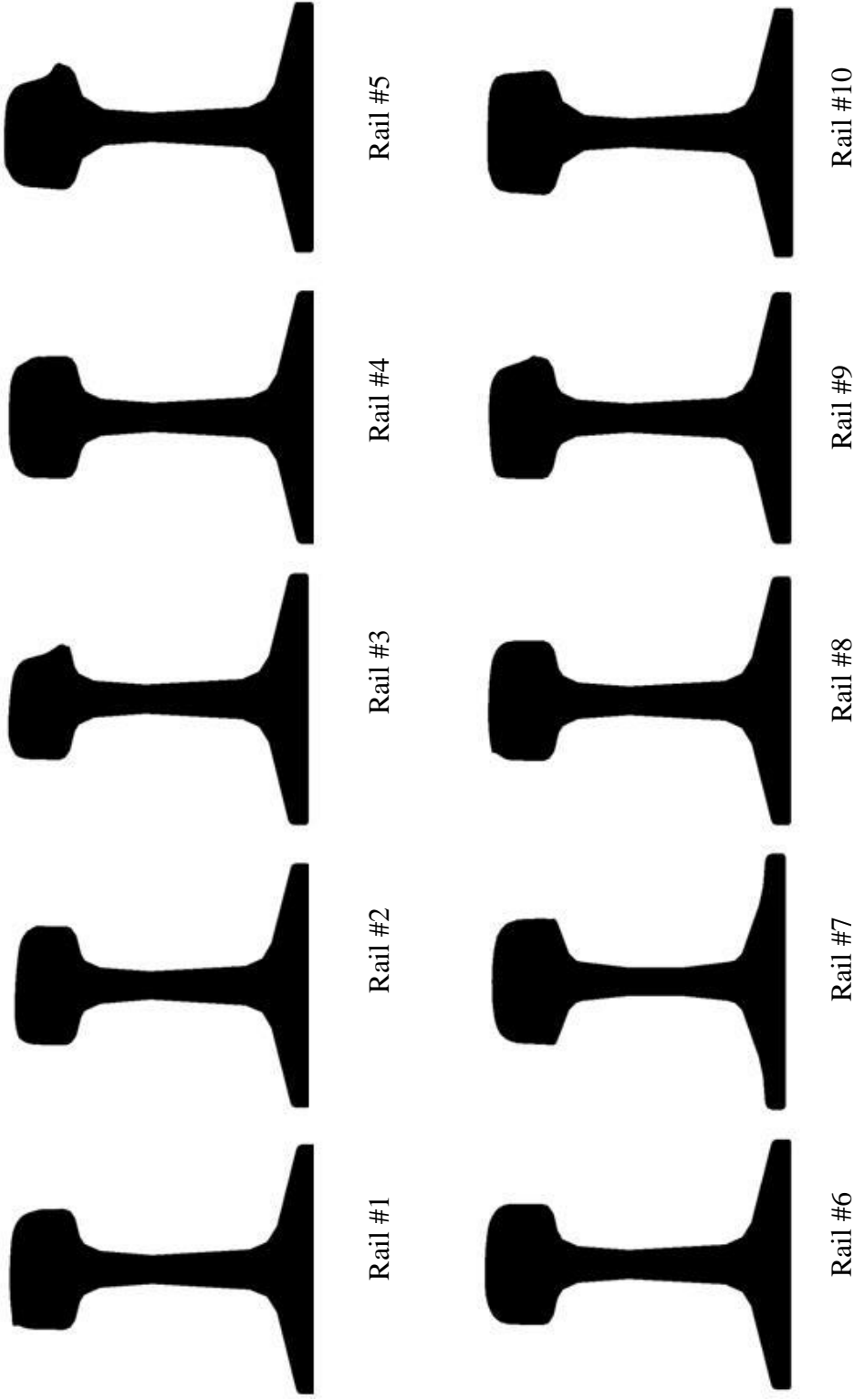tool for measuring the longitudinal stress.

Figure 4.3: TTCI rail profiles.

Table 4.2: Unstressed Rayleigh wave polarization values.

| Rail #	Rail Branding	Rail Side	Pol 1	Pol 2	Pol 3	Pol 4	Pol 5	Average	COV (%)
1	136 RE NKK 1996	F	0.806	0.775	0.800	0.801	0.802	0.797	1.40%
		G	0.723	0.728	0.725	0.727	0.727	0.726	0.25%
2	136 RE CF&I 1987 METRA	F	0.719	0.762	0.751	0.731	0.730	0.738	2.09%
		G	0.741	0.675	0.733	0.735	0.783	0.733	4.71%
3	136 RE VT THYSSEN 1990	F	0.825	0.810	0.819	0.824	0.817	0.819	0.69%
		G	0.585	0.533	0.577	0.467		0.540	8.67%
4	HAYANGE 136 LBS RE 1981	F	0.733	0.729	0.731	0.754	0.724	0.734	1.38%
		G	0.565	0.542	0.541	0.535	0.537	0.544	1.96%
5	141 AB HHC VT DO 2001	F	0.684	0.681	0.699	0.679	0.692	0.687	1.10%
		G	0.703	0.698	0.698	0.704		0.701	0.40%
6	136 RE VT JFE 2005	F	0.694	0.723	0.700	0.719	0.700	0.707	1.62%
		G	0.732	0.749	0.745	0.727	0.732	0.737	1.16%
7	136 RE IH VT T2 2001	F	0.666	0.679	0.643	0.615	0.613	0.643	4.13%
		G	0.717	0.716	0.717	0.718	0.699	0.714	1.02%
8	CORUS MS 1060 E2	F	0.715	0.713	0.714	0.721	0.710	0.715	0.51%
		G	0.697	0.694	0.691	0.691	0.695	0.694	0.34%
9	136-10 CC BETHSTEELTON 1993	F	0.682	0.689	0.706	0.666	0.693	0.687	1.93%
		G	0.663	0.645	0.641	0.645	0.644	0.648	1.21%
10	141 AB VT RMSM 2002-10	F	0.711	0.705	0.715	0.737	0.740	0.722	1.97%
		G	0.777	0.807	0.793	0.770	0.802	0.790	1.79%
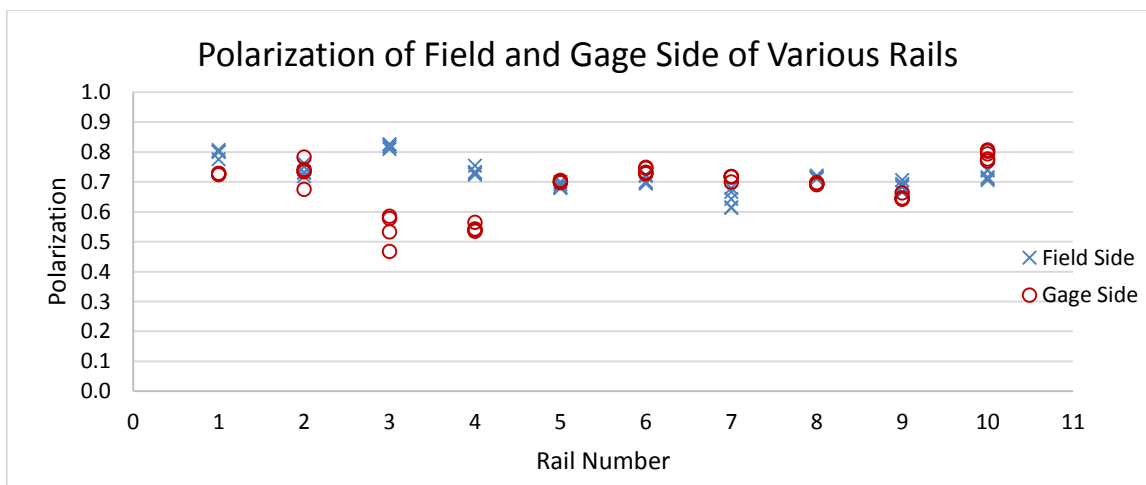
Figure 4.4: Unstressed Rayleigh wave polarization values.

4.4.2 Stressed Rails

For this investigation, four rail surfaces were tested. For the first three surfaces, the Rayleigh wave polarization was measured at five discrete locations chosen to promote higher signal strength. At each location between five and ten excitation waveforms were recorded, with each waveform composed of a 512 cycle average measured by the DPO. This process was repeated for every load, with loads ranging from 5 – 40 T. The fourth surface was measured similarly to the first three, but with measurements performed at only a single location on the rail surface.

The first test condition was the field side of a 136 lb/yd RE rail produced by NKK in Japan. This rail, manufactured in June of 1996, shows moderate surface degradation. The results of this test are displayed in Table 4.3 and Figure 4.5, where Π represents the average polarization of the five to ten measurements taken at each location, $\overline{\Pi}$ represents the average of all measurements taken for the given load, the distance from the excitation source, d, is measured in mm, and the coefficient of variation (CoV) is equal to the standard deviation divided by the average.

Table 4.3: Rayleigh wave polarizations measured on rail surface 1.

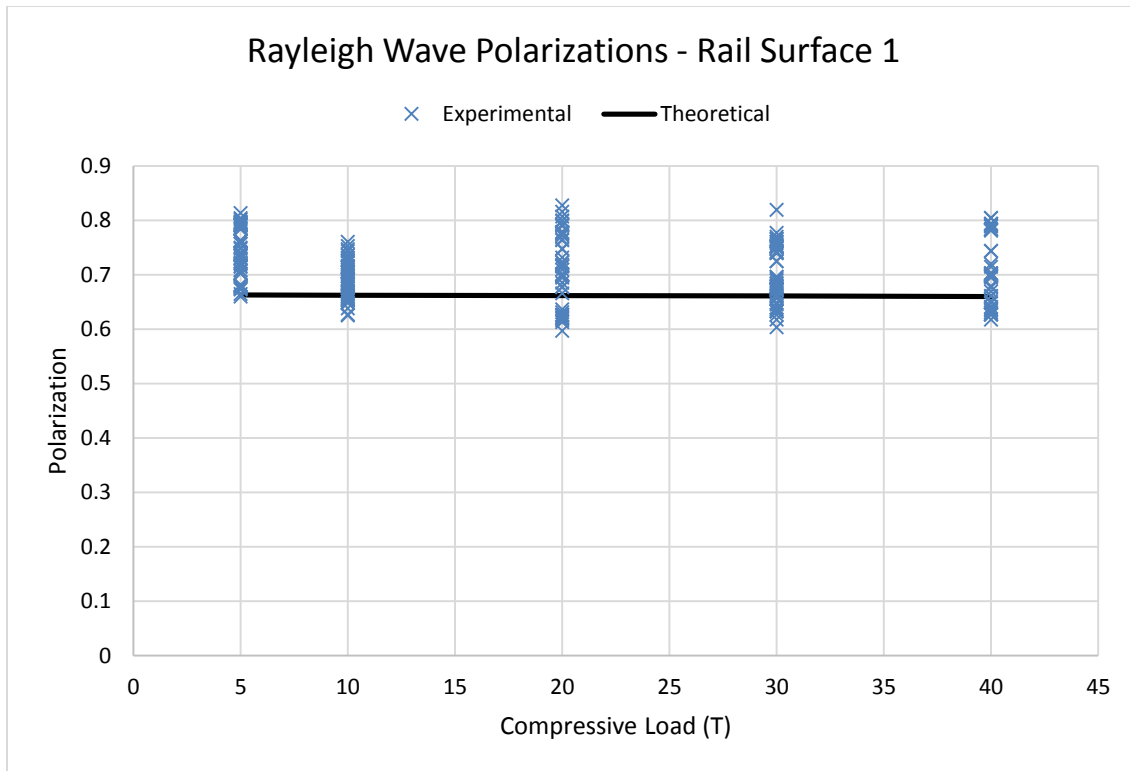| Load (T)	40		30		20		10		5	
	d (mm)	Π	d (mm)	Π	d (mm)	Π	d (mm)	Π	d (mm)	Π
	167	0.644	167	0.635	167	0.790	168	0.732	169	0.675
	174	0.793	169	0.683	170	0.767	173	0.652	177	0.716
	187	0.643	174	0.747	189	0.712	190	0.680	185	0.778
	198	0.773	196	0.671	202	0.621	203	0.705	195	0.795
	210	0.703	202	0.756	205	0.702	206	0.684	212	0.741
$\overline{\Pi}$		0.7022		0.6990		0.7136		0.6916		0.7410
CoV		8.98%		6.85%		8.78%		5.04%		6.11%

Figure 4.5: All Rayleigh wave polarization measurements for rail surface 1.

The second test condition was the gage side of the same NKK rail. This side of the rail showed surface condition similar to the field side. Results are displayed in Table 4.4 and Figure 4.6.

Table 4.4: Rayleigh wave polarizations measured on rail surface 2.

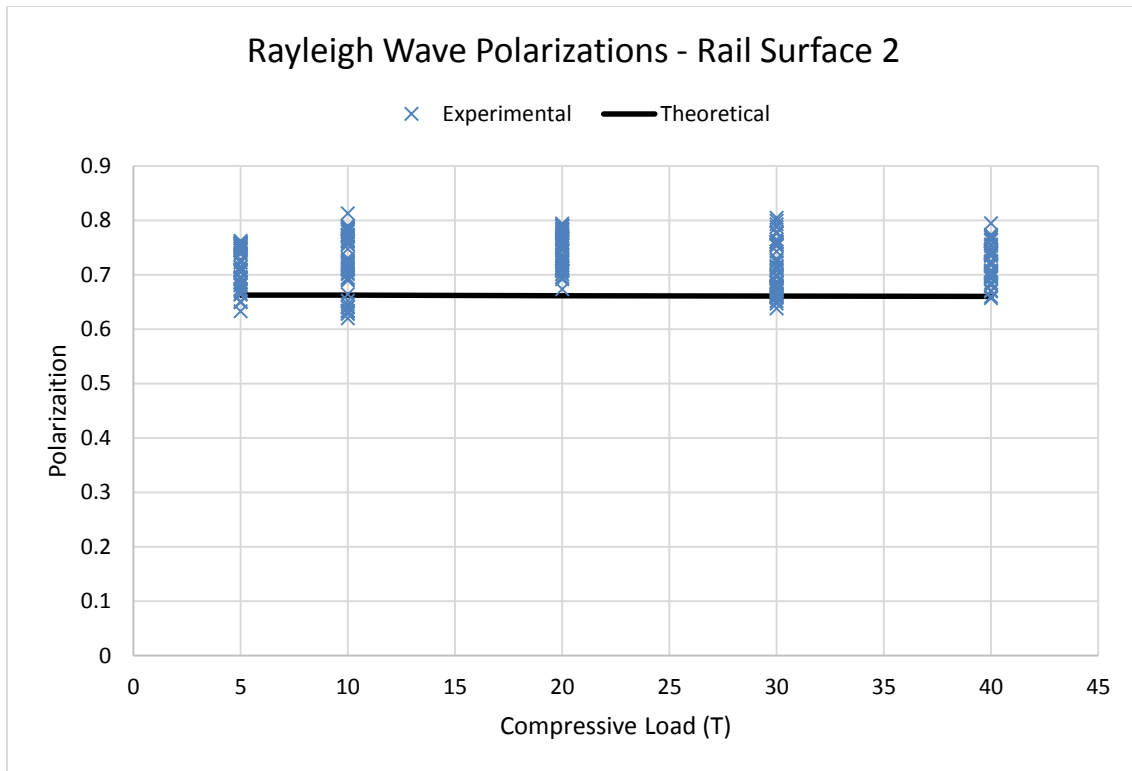| Load (T)	40		30		20		10		5	
	n	*Π*	*n*	*Π*	*n*	*Π*	*n*	*Π*	*n*	*Π*
	1	0.703	1	0.672	1	0.774	1	0.635	1	0.663
	2	0.691	2	0.726	2	0.709	2	0.715	2	0.704
	3	0.742	3	0.677	3	0.751	3	0.773	3	0.749
	4	0.739	4	0.713	4	0.715	4	0.776	4	0.753
	5	0.742	5	0.778	5	0.771	5	0.708	5	0.707
$\overline{\Pi}$		0.7219		0.7131		0.7439		0.7208		0.7166
CoV		4.49%		6.47%		4.42%		7.69%		4.96%

Figure 4.6: All Rayleigh wave polarization measurements for rail surface 2.

The third test condition was the gage side of a 136 lb/yd RE rail manufactured by Colorado Fuel and Iron (CF&I) in August of 1987. This rail surface showed increased degradation compared to the NKK rail. Results are displayed in Table 4.5 and Figure 4.7.

Table 4.5: Rayleigh wave polarizations measured on rail surface 3.

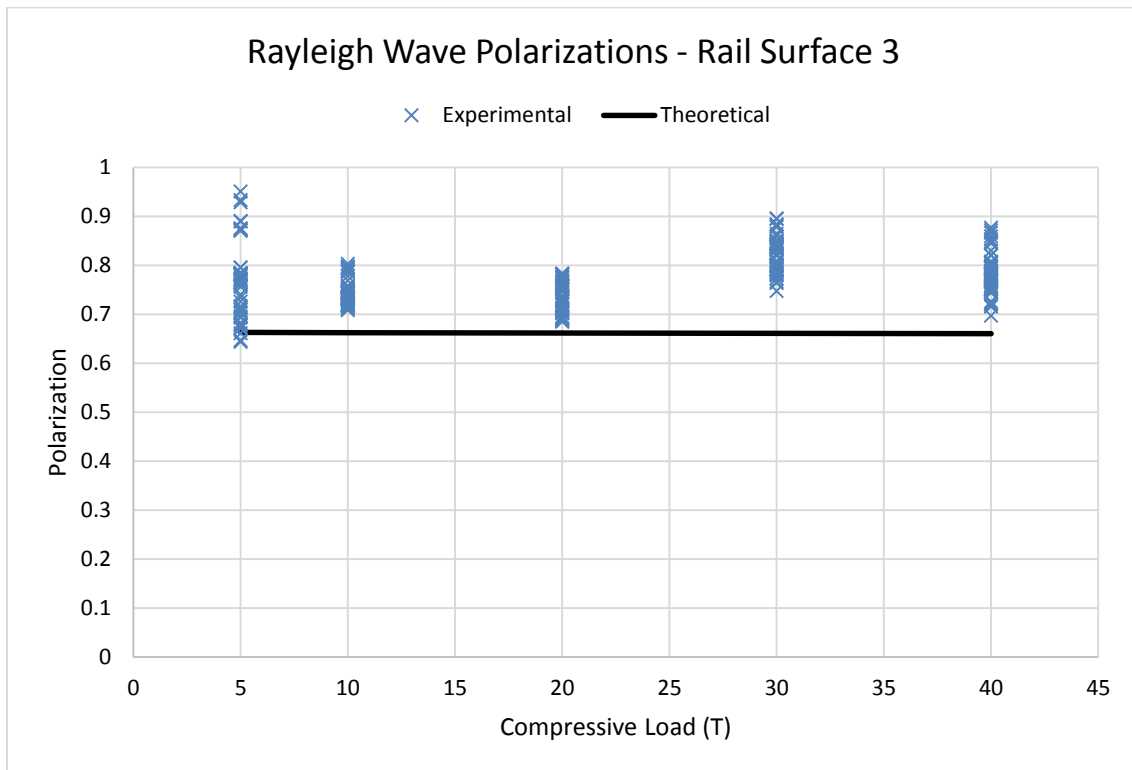| Load (T)	40		30		20		10		5	
	d (mm)	Π	*d (mm)*	Π	*d (mm)*	Π	*d (mm)*	Π	*d (mm)*	Π
	91	0.783	116	0.866	91	0.698	92	0.744	90	0.896
	128	0.753	127	0.799	149	0.712	126	0.740	125	0.710
	164	0.795	148	0.835	163	0.769	163	0.720	197	0.783
	180	0.770	179	0.830	183	0.749	216	0.729	211	0.769
	216	0.817	207	0.784	207	0.741	241	0.789	247	0.676
$\overline{\Pi}$		0.7838		0.8229		0.7347		0.7443		0.7685
CoV		5.27%		4.40%		4.36%		3.45%		10.17%

Figure 4.7: All Rayleigh wave polarization measurements for rail surface 3.

The fourth test condition was a portion of the gage side of the same CF&I rail that was polished to remove rust and other surface imperfections. The target area was polished

44

with vertical strokes to increase reflection for the in-plane LDV. The size of the polished surface was small enough that taking measurements at multiple locations would have been impractical. Results are displayed in Table 4.6 and Figure 4.8.

Table 4.6: Rayleigh wave polarizations measured on rail surface 4.

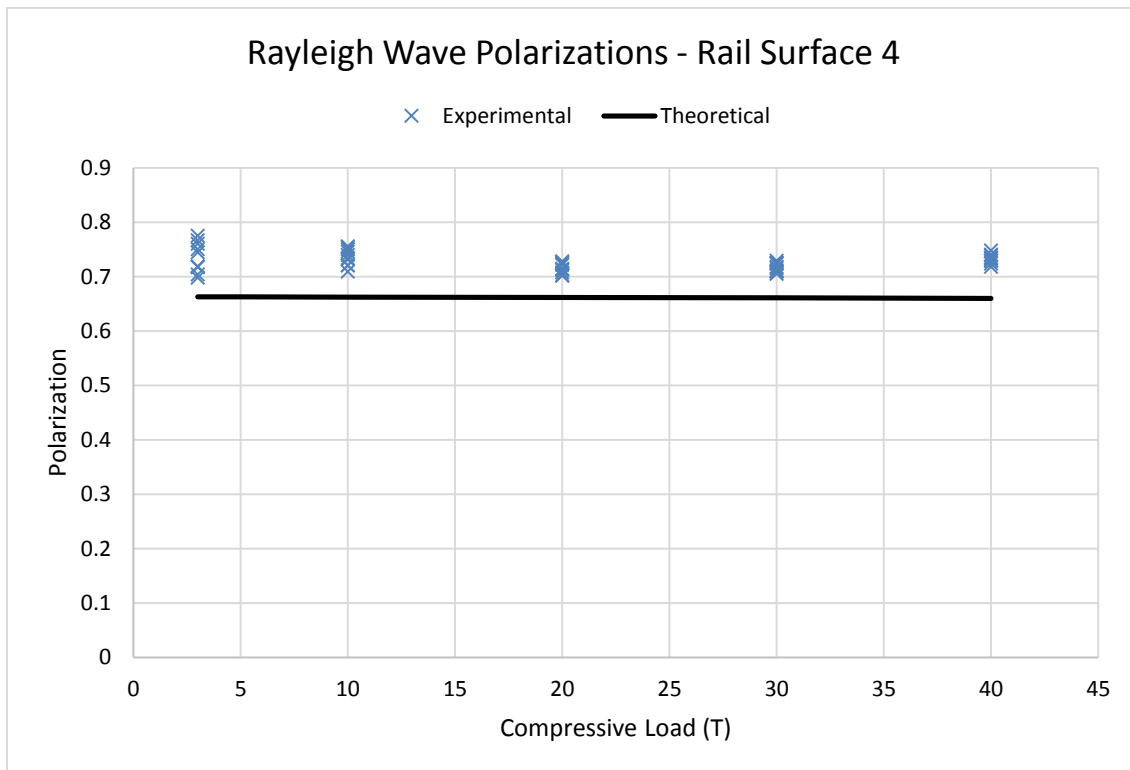| Load (T)	40	30	20	10	3
$\overline{\Pi}$	0.733	0.717	0.715	0.736	0.736
CoV	1.17%	1.14%	1.35%	2.12%	3.72%

Figure 4.8: All Rayleigh wave polarization measurements for rail surface 4.

Figure 4.9 compares the average polarization of each load, $\overline{\Pi}$, for each of the four rail surfaces. Rail surfaces 1 and 2 show polarization values that are fairly close to each

45

other, although less so at lower loads. These results are promising since they suggest that stress measurements can be made from either side of a rail. The dissimilarity could be a result of non-uniform internal stress on the rail that are overpowered by the externally applied stress at higher loads.
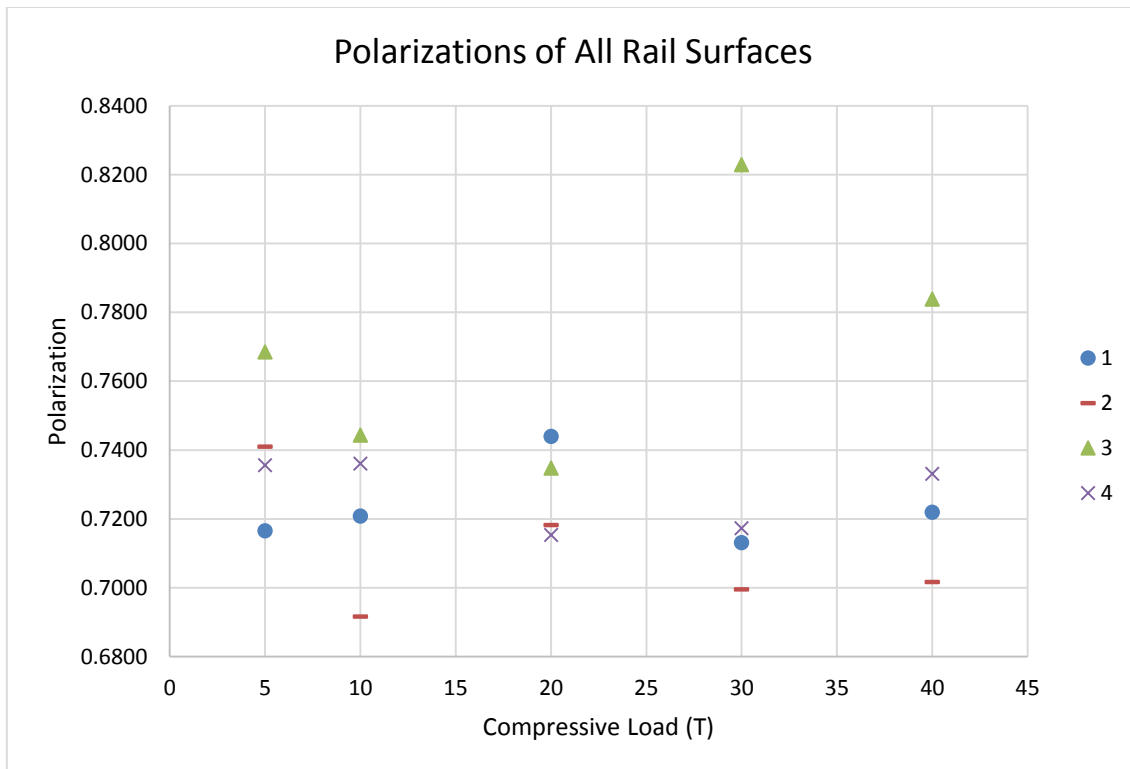

Figure 4.9: Comparison of the average polarizations of all four rail surfaces.

Rail surfaces 1, 2, and 4 provided values that are closer to the theoretical polarizations, while rail surface 3 returned slightly higher polarizations. Since polishing the CF&I rail brought the polarizations back towards the expected values, it can be

concluded that surface condition has a larger impact on the measurement than rail composition does.

In order to determine the optimal placement for the LDV heads in the design of the cart, measurements on the second surface were repeated with the in-plane LDV moved from the typical 45° from the plane of the rail to 60°. This change put the in-plane LDV in a more perpendicular position that increases signal strength, but decreases the component of in-plane vibration measured. Results are displayed in Table 4.7 and Figure 4.10.

Table 4.7: Rayleigh wave polarizations measured on rail surface 2, 60°.

Load (T)	40		30		20		10	
	n	Π	n	Π	n	Π	n	Π
	1	0.713	1	0.709	1	0.761	1	0.760
	2	0.677	2	0.718	2	0.881	2	0.717
	3	0.662	3	0.645	3	0.729	3	0.863
	4	0.791	4	0.667	4	0.752	4	0.814
	5	0.624	5	0.734	5	0.660	5	0.702
$\overline{\Pi}$		0.6936		0.6946		0.7626		0.7712
CoV		9.67%		6.51%		9.88%		8.81%

The CoV's of these polarizations are much higher than the CoV's shown in Table 4.4 of the same rail surface. Therefore the cart was designed with the in-plane LDV head positioned 45° from the web of the rail.
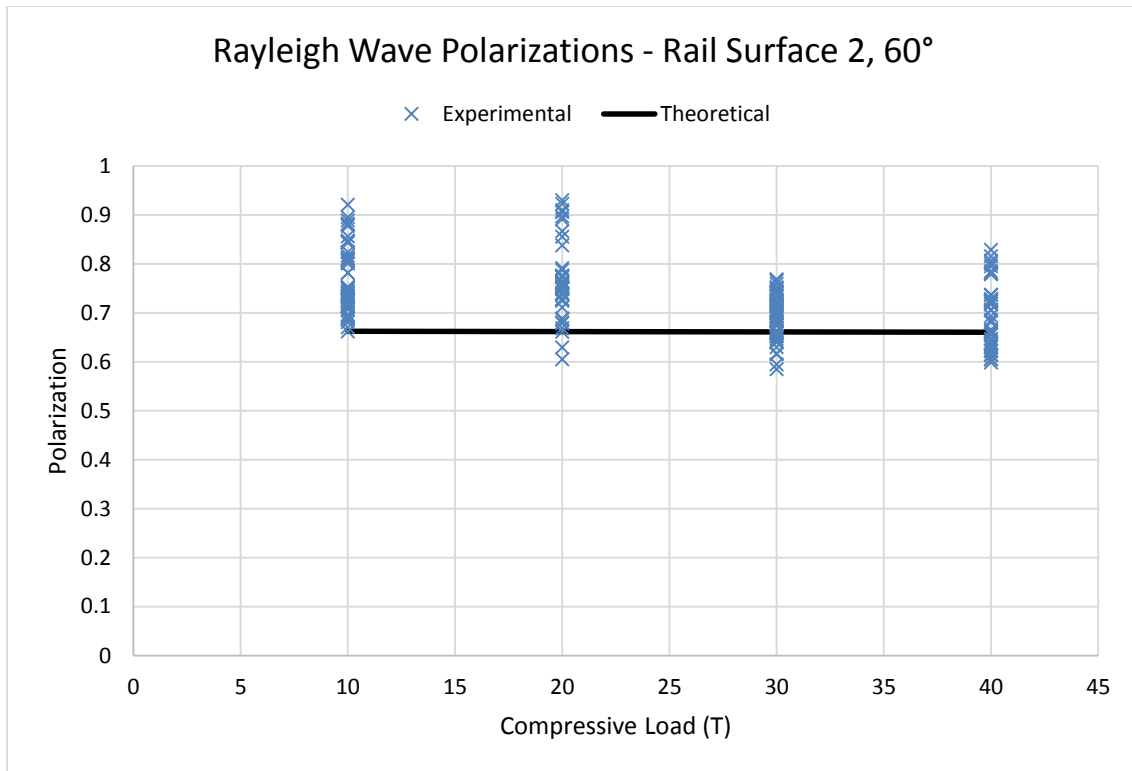
47

Figure 4.10: All Rayleigh wave polarization measurements for rail surface 2 with the in-plane LDV head at 60° from the web of the rail.

5. PROTOTYPE DEVELOPMENT

The first step towards a fully mobile rail stress measurement apparatus is a direct adaptation of these measurement techniques to a stop-and-go system. To this end, a prototype rail stress measurement cart has been developed.

5.1 Design Criteria

During the design phase, a number of goals and critical considerations were established to ensure that the final product was capable of quickly reproducing results comparable to those obtained in a lab environment. A successful mobile rail stress measurement prototype needs:

1. A fully non-contact stress measurement technique

2. Maneuverability on or off tracks

3. Minimal downtime between measurements

4. Modular Framing

5. Protective enclosures for all instrumentation

6. Easy access and control of all instrumentation.

5.1.1 Non-contact Stress Measurement

The biggest change from the lab setup to an in-situ setup is the non-contact Rayleigh wave excitation. By replacing the wedge transducer used in the lab with a pulse laser, the measurement process has become fully non-contact. Not only is this upgrade required for the future use of a moving rail stress measurement system, it also significantly speeds up the stop-and-go system. The non-contact excitation provided by the pulse laser avoids reattaching the wedge transducer at every measurement location. The laser chosen

for this application is a Continuum SLI-10 Nd:YAG laser. The SLI-10 can produce a beam

with a wavelength of 1064 nm, a maximum energy of 450 mJ, and a pulse width of 5-7

ns.

The other end of this fully non-contact stress measurement technique is managed

by the two LDV heads. In order to function at their highest potential, the positioning of

these LDV heads is governed by two restrictions: (1) the distance from the focusing lens

to the surface of the rail must be held at 234 mm and (2) the beam needs to be

perpendicular to the vertical axis of measurement to minimize signal loss, as shown in

Figure 5.1. Both of these restrictions represent a challenge in transitioning to the field from

the idealized environment of a lab.

According to the 4.1-p of the AREMA Manual for Railway Engineering

(American Railway Engineering and Maintenance-of-Way Association, 2014), rail gage

"shall be 4'8-1/2" between point 5/8 inch below the top of rail on the two inside edges of

the rails." In practice however, the tolerance of this measurement varies more than what

is permissible for the LDV head distance. To account for this, the LDV heads have been
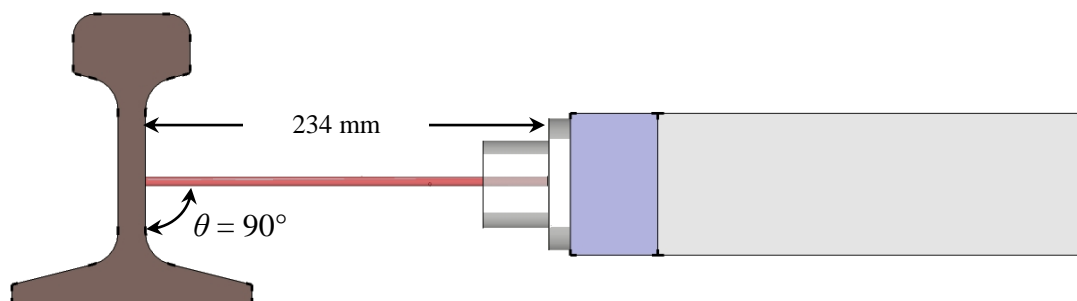

Figure 5.1: LDV head position restrictions.

designed to translate along the axis perpendicular to the web of the rail, which allows the distance to be set for each measurement.

In order for the LDV measurement beam to be perpendicular to the web of the rail, the LDV heads must sit below the top of the rail while making measurements, as seen in Figure 5.1. As the cart travels down the tracks, it will encounter frog guard rails, turnouts, road crossings, signal wires and boxes, and ballast that would interfere with anything below the top of the rail. For this reason, standard AAR practice states that all rail measurement vehicles maintain at least 2-¾ in. clearance above the top of the rail while in motion (American Association of Railroads, 2014). To reconcile this issue, the LDV heads have been mounted to a pair of rotatable arms that allow the LDV head housing unit to be easily moved out of the way while the cart is moving between measurement points, as shown in Figure 5.2.
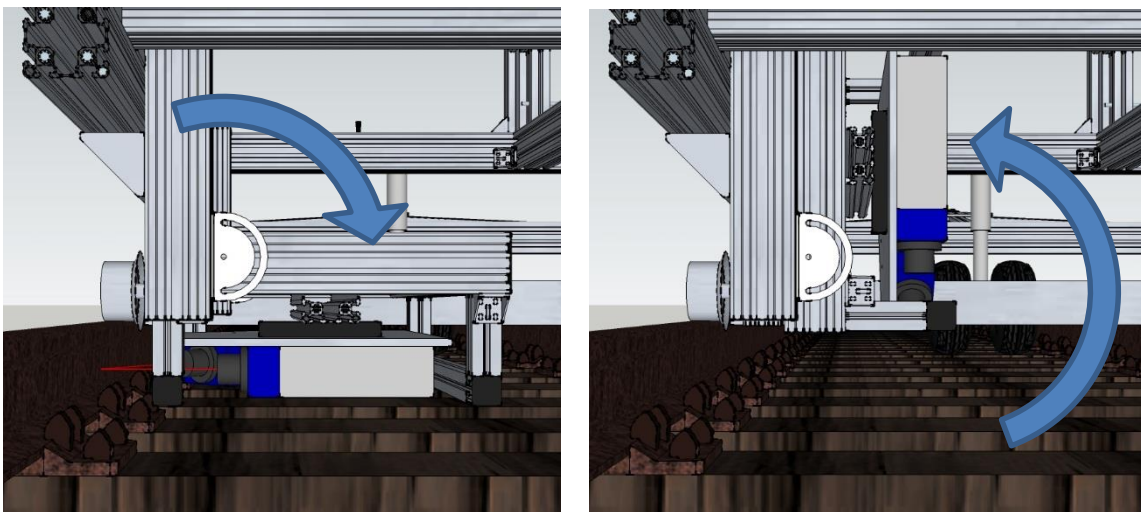

Figure 5.2: LDV heads shown in (a) measurement position and (b) travel position.

51

5.1.2 Maneuverability on or off tracks

In the field, this cart will spend much of its life traveling along rails. However to aid in transporting the cart to measurement sites, it has been designed to be capable of traveling off tracks as well. For this reason, the primary rear axle, located beneath the main instrumentation cabinet, is a standard 5 ft trailer axle with pneumatic wheels. These air-filled tires, which will support the back of the cart whether on or off tracks, help cushion any bumping or jostling that could damage the equipment. While in transit to rails, the front of the cart is designed to be carried by a leveling jack equipped with a pair swiveling pneumatic wheels. The height of these wheels can be adjusted by a crank, which allows them to be moved up out of the way when the cart is on rails. With jack wheels disengaged, the front of the cart will rest instead on an aluminum railroad dolly. An additional set of track wheels located at the rear can be lowered to keep the primary rear axle aligned with the tracks.

Transferring the cart to rails is designed to occur at road crossings. Starting from a position perpendicular to the tracks, the cart may be backed down the tracks until the rear track wheels are engaged. Then, the front of the cart may be aligned with the tracks, and the jack wheels raised until the load is supported by the front track wheels. This process is depicted in Figure 5.3.
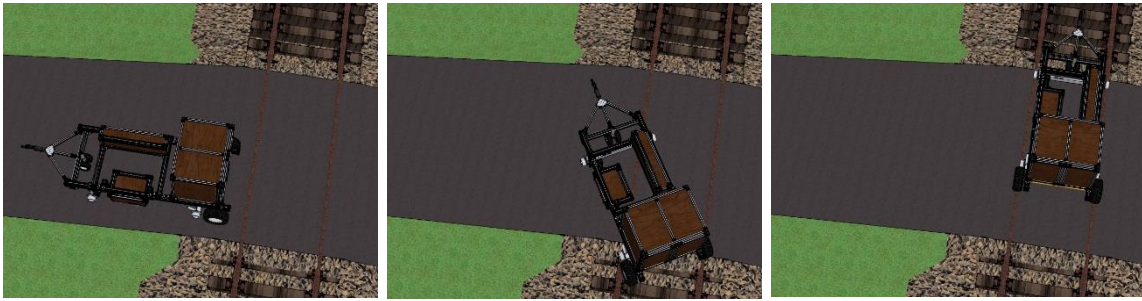
Figure 5.3: Positioning the cart onto the tracks.

5.1.3 Minimal Downtime Between Measurements

In order to be effective, the measurement apparatus needs to be easily moved down the track between measurement points. The most cost effective way to accomplish this is by either pushing or pulling the cart, as opposed to using a self-propelled cart. Early designs for the cart included handles, but eventually these were discarded in favor of a towing connection which allows the cart to be pulled behind a hi-rail vehicle. This removes the need to manually move the cart, and also allows the generator that powers the instrumentation to be stored in the bed or trunk of the vehicle. By isolating the generator from the lasers, it no longer introduces additional vibration into the measurements. This decision also introduced a minor complication. The hitch height of hi-rail vehicles is unique to each, but the cart needs to stay level so that both front and rear track wheels remain engaged and so that the water cooling system in the Nd:YAG laser CPU can function. Therefore, an articulated trailer hitch was chosen over the traditional ball hitch to allow for free rotation about all three axes of the hitch and to accommodate any hitch height.

5.1.4 Modular Framing

While a significant effort went into to designing the measurement apparatus to handle any difficulty encountered in the field, it was recognized that modifications may become necessary after building the cart. For this reason, Bosch aluminum framing was chosen to make up the structure of the cart. These extruded aluminum beams are designed to be cut to length and then bolted to one another. Because these connections consist of T-shaped bolts fitting into channels that run the length of each member, they require no machining, and minor adjustments to account for alignment heights or unforeseen impediments are simple.

The stocky 90mm x 90mm members, shown on the left in Figure 5.4, were used for any longer span and to support elements where vibration control was critical, such as the LDV heads. The rest of the members, typically needed for geometry but not for
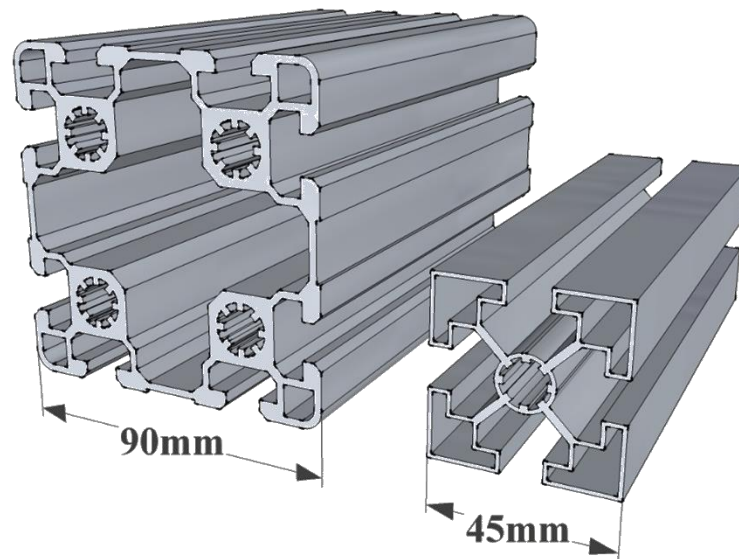

Figure 5.4: Extruded aluminum profiles.

54

structural support, were chosen to be the 45mm x 45mm profile shape. Since the smaller profile is scaled down from the larger by exactly a factor of two, these member types worked well together—allowing 45mm x 45mm members to frame into adjacent slots in a single 90mm x 90mm member.

5.1.5 Protective Enclosures for All Instrumentation

Most of the instrumentation used in the experimental setup is designed for the low-dust, low-moisture environment of a lab. To increase their lifespan in a field environment, the instruments will be stored in enclosed housings. These housing units consist of walls made from a water resistant, film faced plywood secured into the channels of the framing members with a Bosch weather stripping. This system will help keep out dust and debris encountered in the field, provide a barrier against water should the unit get caught out in the rain, and protect the instruments from direct sunlight. One challenge introduced with this choice of enclosure is that any framing channels used for plywood panels cannot be used for bolted connections. This difficulty is another reason the 90mm x 90mm profile shape made up the majority of the framing members in the design. With two slots per face, one can be occupied by a plywood panel and the other can be used to secure the member.

In total there are three instrument housing units. The largest, located at the rear of the cart, functions as a pair of 19 in., 20 RU (35 in. tall) rack cabinets that hold the oscilloscope, the two LDV controllers, the Nd:YAG power supply unit, and the HeNe alignment laser controller. Both sides can be accessed independently and contain space for additional devices should the need arise. The second housing unit contains the Nd:YAG and HeNe laser heads. Since there is no restriction on the distance between the

measured rail and the Nd:YAG laser, it is located on the right side of the cart—opposite the measured rail. These laser heads are accessed from the side of the cart by a door that opens vertically. From this opening, the mirrors controlling the direction of the excitation beam can be adjusted. The final instrument enclosure houses the LDV heads and their associated hardware. As mentioned in Section 5.1.1, this housing can be rotated into measurement position or out of the way during transit. Due to the critical clearance dimensions around the LDV heads in their measurement position, this housing unit has two panels that bolt on to the outside face of their framing member as opposed to fitting in the member channel. This allows the LDVs to make measurements on the lower half of the rail web without interference from the rail road ties.

5.1.6 Easy Access and Control of All Instrumentation

Lastly, the process of conducting rail stress measurements would be expedited if all inputs and common adjustments could be performed from a single location on the cart. All of the instrument controls are localized to the double 19 in. rack cabinet, however each measurement will need to include an adjustment of the lateral position of the LDV heads, as discussed in Section 5.1.1. To facilitate this frequent adjustment, the LDV heads have been affixed to a motorized translation stage with a 50 mm travel distance whose control unit is also located in the main instrument cabinet. Additionally, a webcam has been placed between the LDV heads so that the necessary adjustments can be monitored from the same location. Once the measurement process has begun, any measurements performed along a stretch of rail clear of obstructions can be completely monitored and controlled from the main instrument rack.

5.2 Modeling

Once the essential standards of the design were established, a digital model was created. SketchUp was chosen for this task for its power and ease of use among free 3D modeling software. Modeling the design allowed for many problems and inconsistencies to be caught and corrected before changes became costly. Additionally, rendering 3D models proved invaluable when consulting with TTCI personnel whose experience with railroad measurement devices helped keep the apparatus practical. Preliminary designs of the cart included only the flanged wheels required for rails, as shown in Figure 5.5.
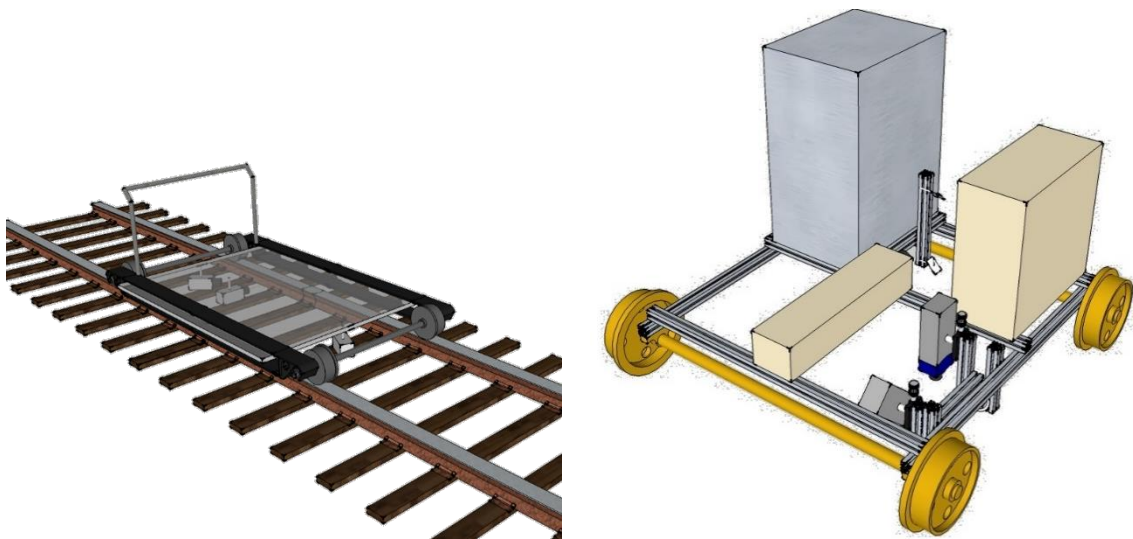
Figure 5.5: Preliminary cart designs with only flanged wheels.

Once the protective panels were added to the model, it became apparent that space limitations would require the laser heads to be separated from the rest of the instrumentation, as shown in Figure 5.6a. Figure 5.6b illustrates early attempts to increase off-rail maneuverablity by including four full-size trailer tires, four moveable trackwheels, and a push handle. Later, the front trailer axle was replaced with a jack and a pair of fixed trackwheels, seen in Figure 5.6c and Figure 5.6d.
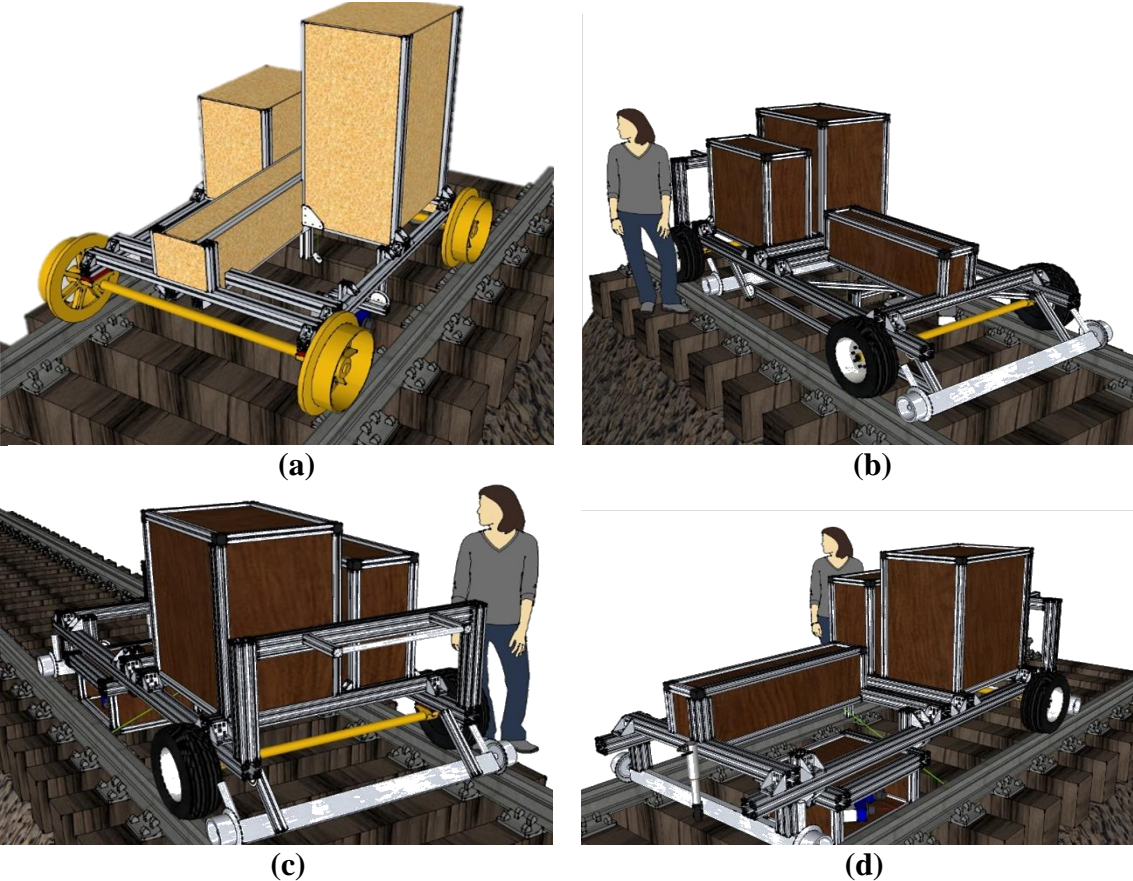

(a)   (b)

(c)   (d)

Figure 5.6: Iterative measurement cart designs.

To increase the compatibility with future upgrades, both sides of the main instrument housing units were altered to accommodate standard 19 in. rack cabinet mountings, as shown in Figure 5.7a. Additionally, after consulting with TTCI personel, it was decided to incorporate a towing connection for use with hi-rail vehicles. Eventually, this change led to the removal of the push handle, which conflicted with access to the main instrument cabinets.
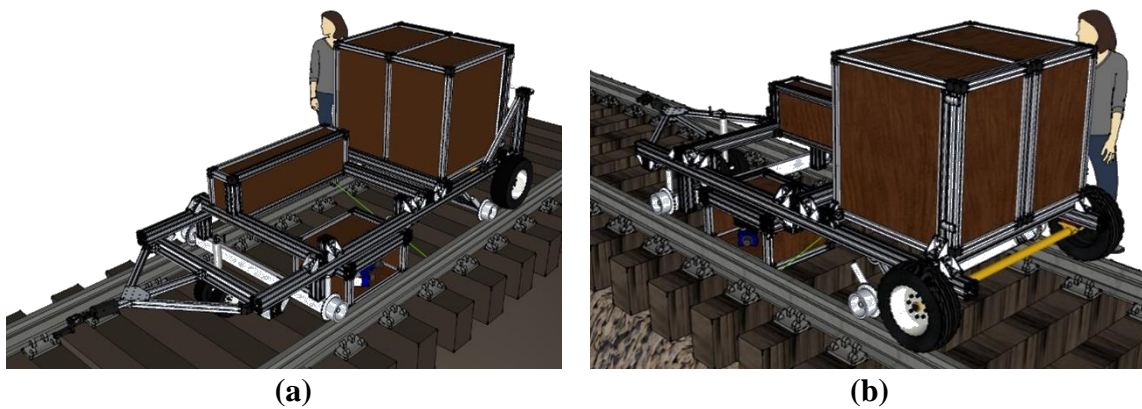

(a)   (b)
Figure 5.7: Digital models of the cart showing (a) the addition of the towing connection and (b) the removal of the push handle.

The final design of the cart, shown in Figure 5.8 through Figure 5.14, represents the point at which all of the design criteria had been met and no additional problems were foreseen.
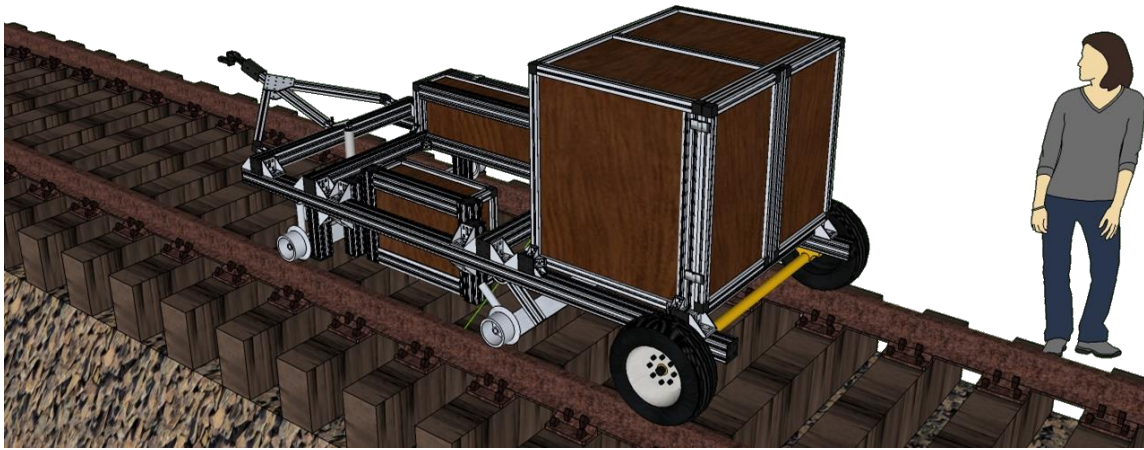
Figure 5.8: Final pre-construction design of the cart shown with the LDV housing raised in travel position.
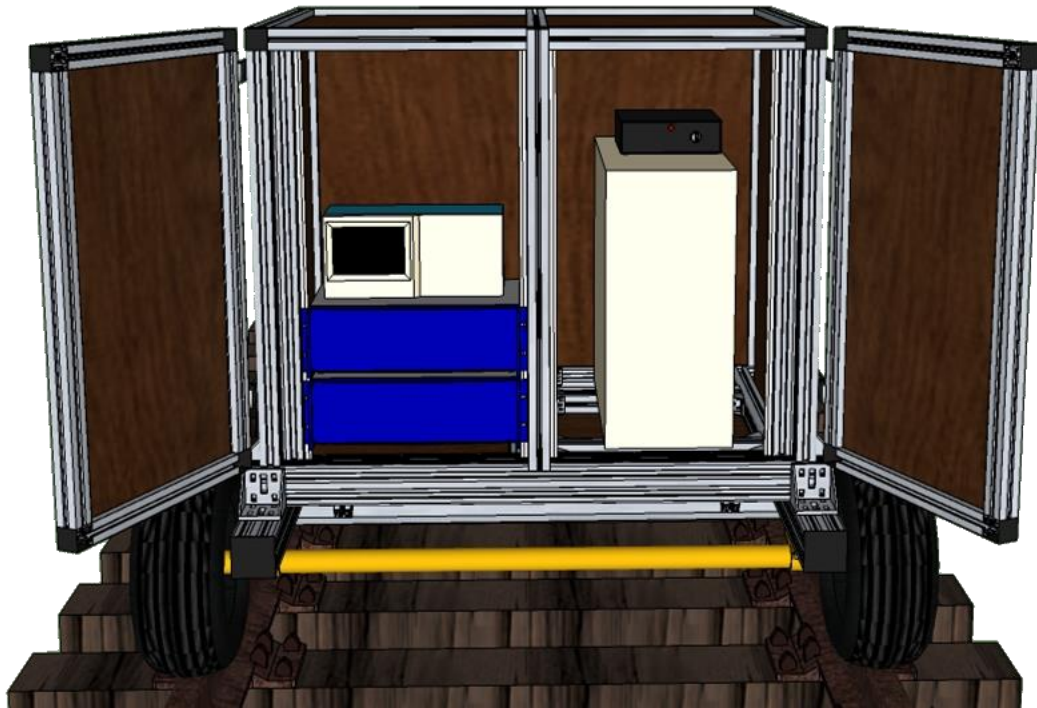

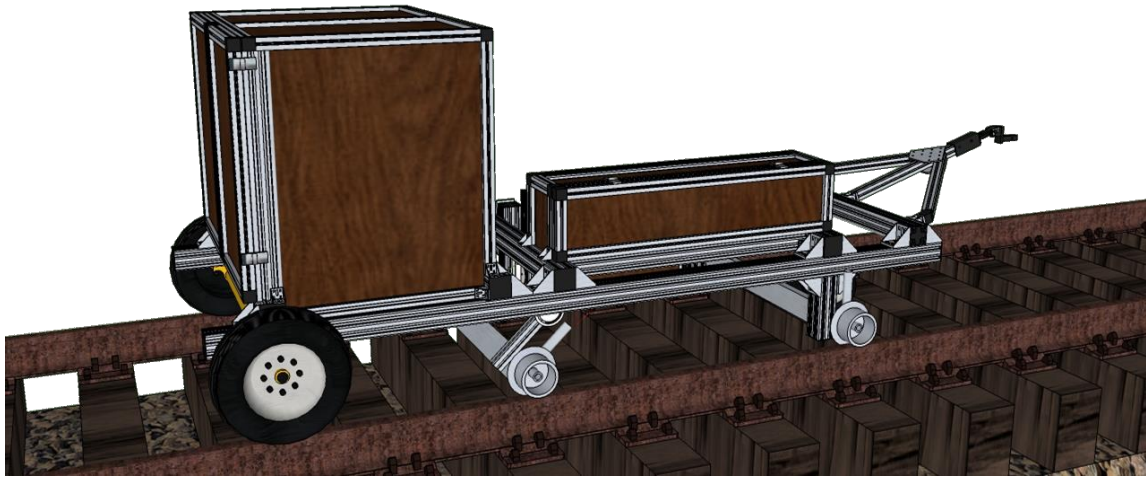**Figure 5.9: View of the equipment in the instrumentation cabinets.**
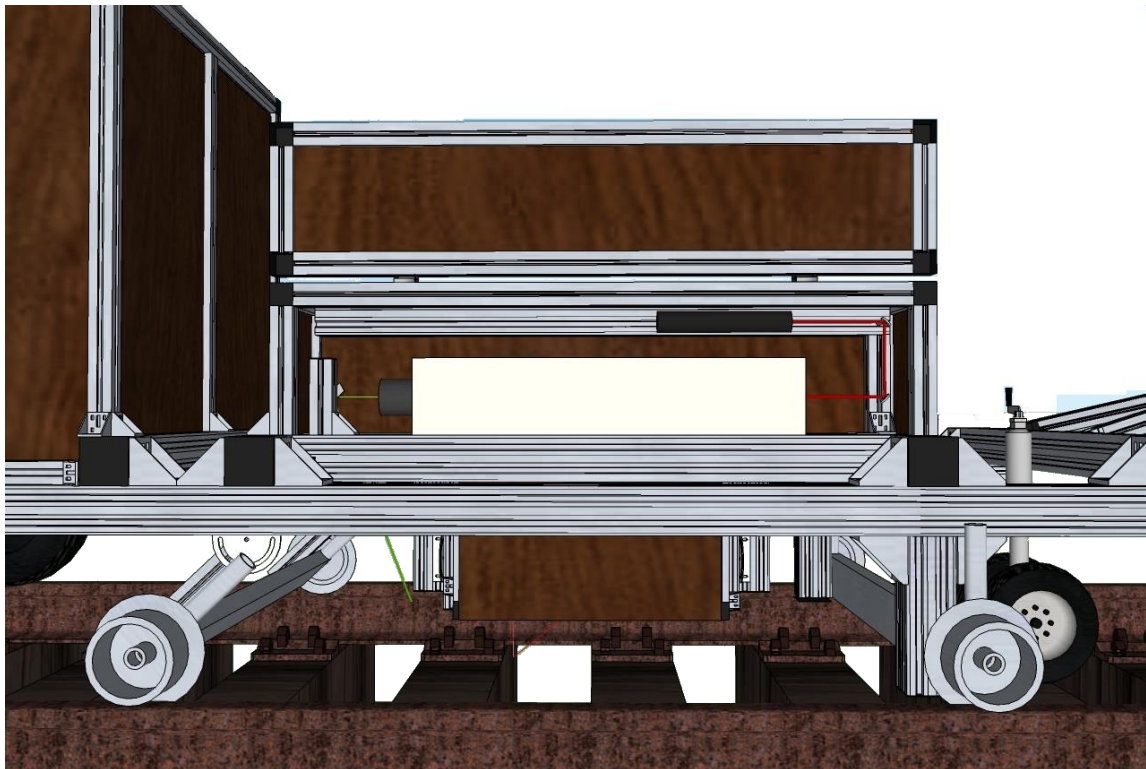
Figure 5.10: Side view of the final cart design.

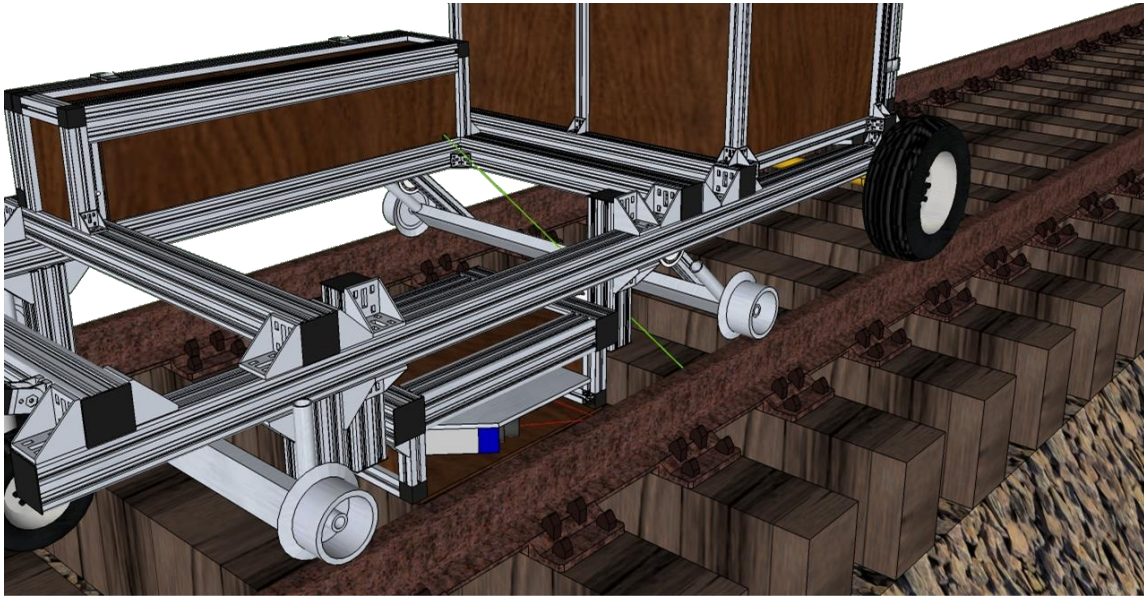**Figure 5.11: Nd:YAG and HeNe laser heads.**

Figure 5.12: LDV housing unit shown lowered into measurement position.
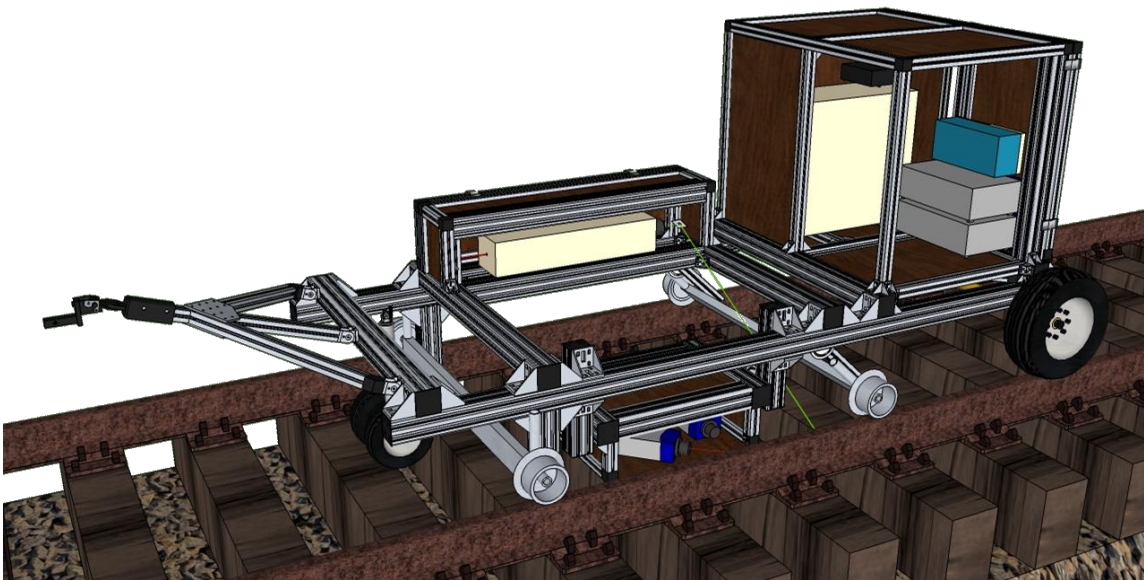

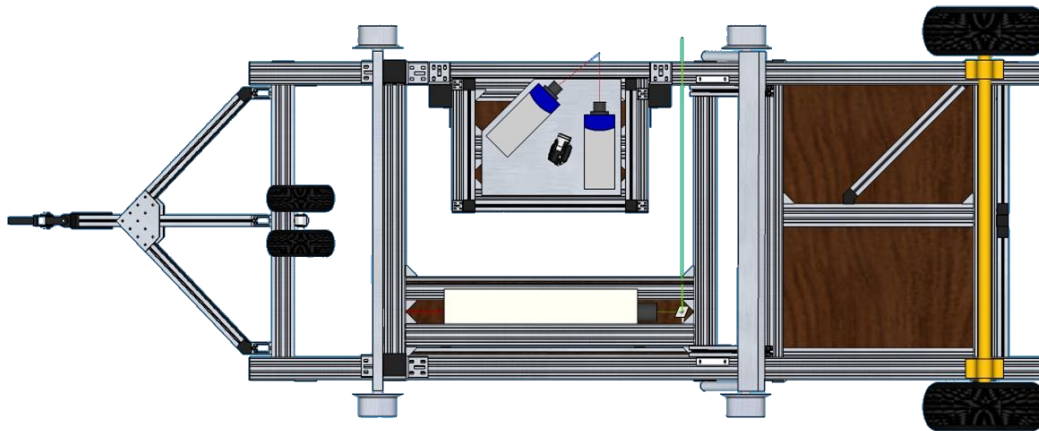**Figure 5.13: Cart instrumentation.**

Figure 5.14: Bottom view of the cart showing the location of the LDV heads and the beam path of the Nd:YAG laser.

5.3 Construction

Construction of the cart began as soon as the final design was established. The primary frame of the cart is constructed from Bosch framing pieces as shown in Figure 5.15. This means that any components not issued by Bosch needed to be modified in order to be compatible with the Bosch profiles. Holes were drilled in all three axles to accommodate Bosch's T-bolts, while the jack has been bolted around a 90mm x 90mm member to a mounting plate. Originally the jack was equipped with small plastic tires, but these were replaced with pneumatic tires that are better suited for the cart's environment. The trailer axle and modified side mount jack can be seen attached to the frame in Figure 5.16.
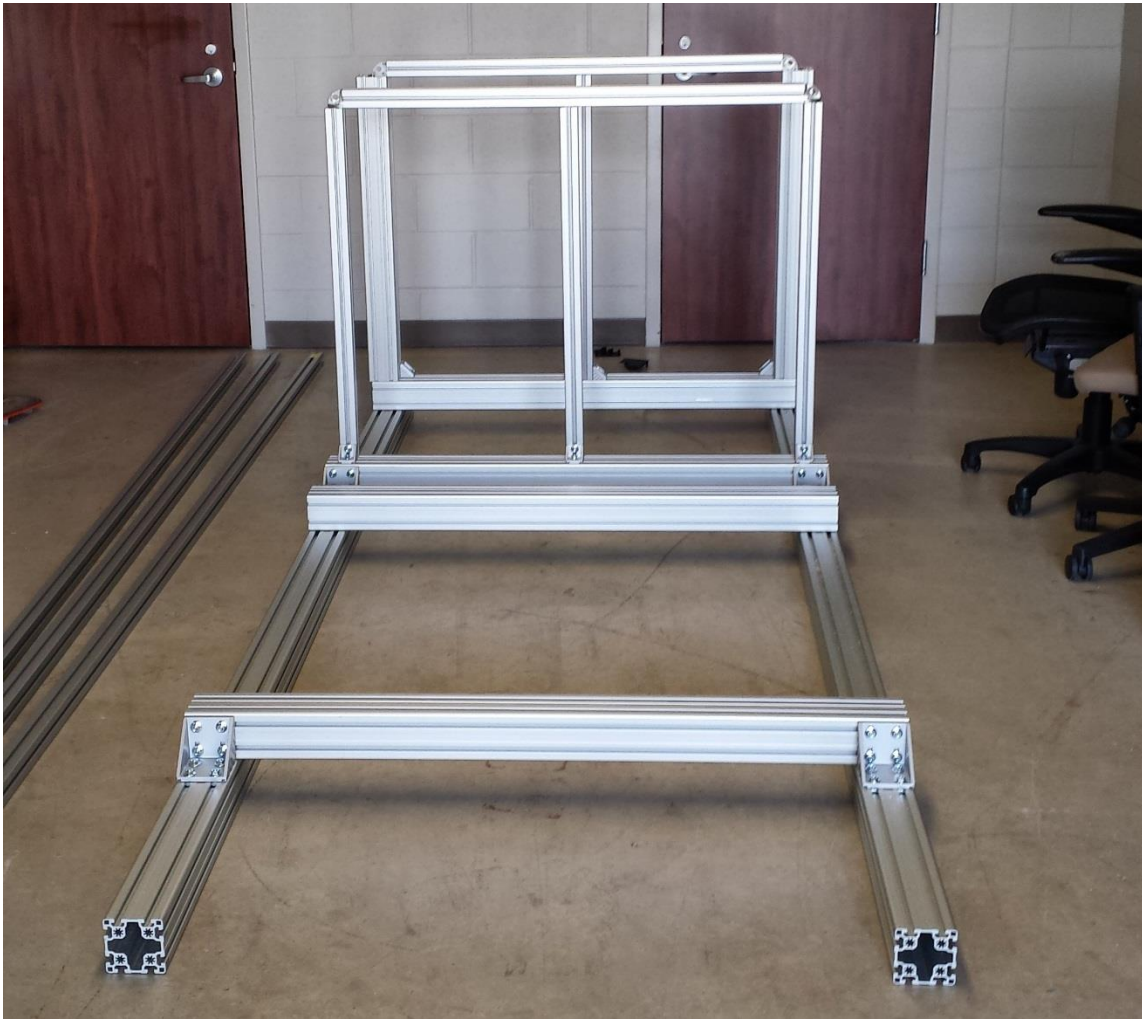
Figure 5.15: Bosch extruded aluminum members make up the frame of the cart.

The LDV heads and webcam are attached to a 10 mm plate. The aluminum plate was cut to size with a band saw, and holes for each component were drilled with a mill. The aluminum plate is suspended from the motorized translation stage, which is attached to a 10mm thick aluminum connector that holds the entire LDV translation apparatus to the LDV housing frame. This attachment detail is shown in Figure 5.17.

Figure 5.16: Primary cart frame attached to the trailer axle and side mount jack.

Figure 5.17: Front view of the LDV housing unit shows the Thor MTS50 motorized translation sandwiched between the two 10 mm aluminum mounting plates.

The HeNe laser head is attached to the inner slot of a 90mm x 90mm member with a cage mount system. This allows the laser to be positioned anywhere along the length of its housing unit. The Nd:YAG laser head is supported by its own feet and held in place by a series of gussets, as shown in Figure 5.18.

Figure 5.18: Opened Nd:YAG housing unit.

The Nd:YAG PSU is similarly locked in place by a series of 45 mm gussets and members. The rest of the instrumentation is bolted to the 19 in. rack rails, which can be seen in Figure 5.19b.

The completed cart is shown in Figure 5.19 and Figure 5.20.

(a)

(b)

(c)

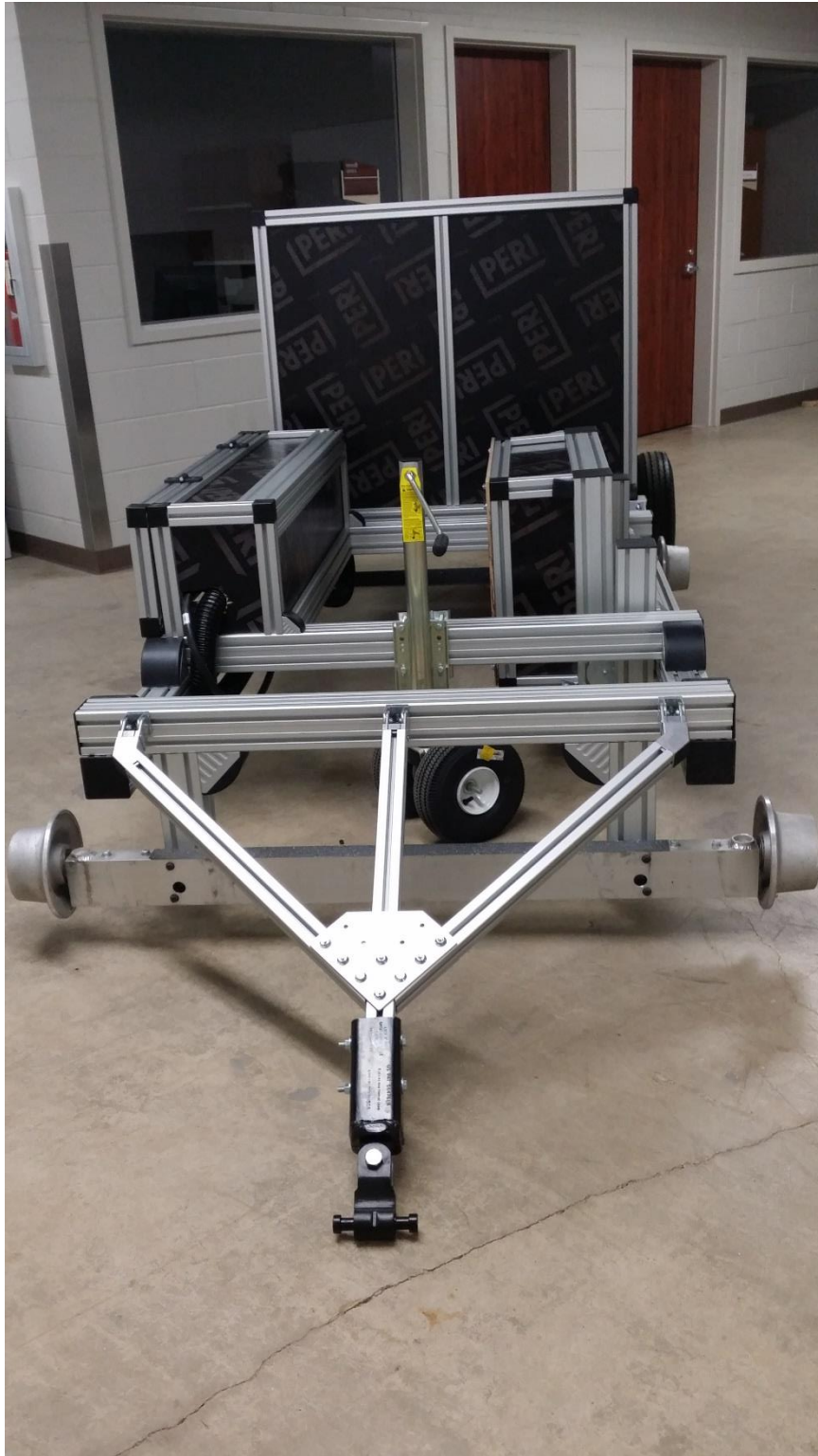**Figure 5.19: Cart prototype.**

Figure 5.20: Final Cart prototype.

6. CONCLUSIONS AND FUTURE WORK

This research has set out to develop a longitudinal rail stress measurement apparatus prototype for use in the field. This prototype measures stress by analyzing Rayleigh wave polarization, which is recorded by a pair of laser Doppler vibrometers. To better predict the accuracy of this technique in the field, a study was performed on the effects of rail condition on the Rayleigh wave polarization measurement. This study found that a rail's surface condition affects the measurement results more than the rail's composition or history. The polarization change from rail surface 3 to rail surface 4 indicates that surface condition plays an important role in this, but other factors could include temperature, non-uniform internal stress, and edge effects caused by using small rail samples.

With these facets of the polarization measurement technique examined, a series of guidelines was established that would allow this measurement to be recreated outside the lab. These essentials, including use of a fully non-contact stress measurement technique, maneuverability on or off tracks, minimal downtime between measurements, modular framing, and protected and easily accessed instrumentation, were expressed through an iterative 3D modeling process. This lead to a design that adhered to these guidelines and culminated in the construction of a functioning prototype.

This prototype will enable measurements previously carried out only in the lab to be performed on any rail. This accessibility will allow the measurement of a wider range of rails which will further establish the efficacy of this technique.

For future work on this topic, it is first suggested that a field test of this prototype be performed. By comparing measurements performed in the field with data collected in the lab, the importance of some variables, such as end effects, can be established.

Additional future work includes an analysis of solutions to current barriers against an in-motion measurement. Some obstacles, such as the LDV heads interfering with rail clearance restrictions, will need to be resolved before an in-motion system can be realized. Others, like instrument vibrations and laser misalignments induced by vehicle motion, are inherent in a mobile measurement situation and will need to be accounted for as the in-motion system develops.

REFERENCES

American Railway Engineering and Maintenance-of-Way Association (2014). *Manual for Railway Engineering*, 5-4-3.

Association of American Railroads (2014). *AAR Manual of Standards and Recommended Practices.* Washington, DC.

Bray, D. E. (2002). "Ultrasonic Stress Measurement in Pressure Vessels, Piping, and Welds." *Journal of Pressure Vessel Technology*, 124 (3), 326-335.

Bray, D. E., and Leon-Salamanca, T. (1985). "Zero-Force Travel-Time Parameters for Ultrasonic Head-Waves in Railroad Rail." *Material Evaluation*, 43, 854-863.

Damljanovic, V. and Weaver, R.L. (2005). "Laser Vibrometer Technique for Measurement of Contained Stress in Railroad Rail." *Journal of Sound and Vibration*, 282, 341-366.

Djayaputra, F. (2010). "Determination of Longitudinal Stress in Rails," Masters Thesis, Texas A&M University.

Duquennoy, M. and Ouaftough, M. and Ourak, M. (1999). "Ultrasonic Evaluation of Stresses in Orthotropic Materials Using Rayleigh Waves." *NDT&E International*. 32(4), 189-199.

Egle, D. M. and Bray, D. E. (1979). "Application of the Acousto-Elastic Effect to Rail Stress Measurements." *Material Evaluation*, 37, 41-55.

Ghita, E., Nagi, M., and Carabas, I. D. (2010). "The residual state of stress in old railroads for public transport by tram vehicles," *Annals of DAAAM Proceedings*, pp. 1109-1110.

Graff, K.F. (1991). *Wave Motion in Elastic Solids*. Dover Publications Inc., New York.

Hayes, A.P. (2008). "MAPS-SFT, a New Tool in the Infrastructure Manager's Toolbox." MAPS Technology Ltd, UK.

Hirao, M., Ogi, H., and Fukuoka, H. (1994). "Advanced ultrasonic method for measuring rail axial stresses with electromagnetic acoustic transducer," *Research in Nondestructive Evaluation*, vol. 5, pp. 211-223.

Hurlebaus, S. (2005). "Smart Structures." Manuscript, Zachry Department of Civil Engineering, Texas A&M University.

Husson, D., Bennet, S. D., Kino, G. S. (1982). "Measurement of Surface Stresses Using Rayleigh Waves." *Ultrasonic Symposium*, 889-892.

Junge, M. (2003). "Measurement of Applied Stresses Using the Polarization of Rayleigh Surface Waves," Masters Thesis, University of Stuttgart.

Junge, M., Qu, J., and Jacobs, L. J. (2006). "Relationship between Rayleigh wave polarization and state of stress." *Ultrasonics 44,* 233-237.

Kish, A., and Samavedam, G. (2005). "Improved destressing of continuous welded rail for better management of rail neutral temperature." *Journal of the Transportation Research Board*, *1916*, 56-65.

Kish, A., Samavedam, G., and Al-Nazer, L. U.S. Department of Transportation, Federal Railroad Administration. (2013). *Track buckling prevention: Theory, safety concepts, and applications* (DOT/FRA/ORD-13/16). http://www.fra.dot.gov/eLib/details/L04421

Lonsdale, C. P. (1999). "Thermite rail welding: History, process developments, current practices and outlook for the 21st century," *AREMA Conference Proceedings*.

Pao, Y. H., and Sachse, W., and Fukuoka, H. (1984). "Acoustoelasticity and Ultrasonic Measurements of Residual Stresses." *Physical Acoustics*, 17, 61-143.

Phillips, R. R. (2012). "Ultrasonic Methods for Rail Inspection," http://gradworks.umi.com/35/45/3545395.html Dissertation, University of California, San Diego.

Rose, L. (1999). *Ultrasonice Waves in Solid Media.* Cambridge University Press, Cambridge, UK.

Sadovi C. and Danna, J. (2012). "Train derails, bridge collapses near northbrook-glenview border," http://articles.chicagotribune.com/2012-07-04/news/chi-train-derails-in-near-northbrookglenview-border-20120704_1_train-cars-train-derails-freight-train. Chicago Tribune, 2012.

Tunna, J. (2000). "Vertical Rail Stiffness Equipment (VERSE) TRIALS." *Letter Report for Vortex International*, Transportation Technology Center Inc. (TTCI), Pueblo, CO.

VERSE. (2012). *Innovation in Rail Track Safety*. http://www.vortok.com/uploads/image s/Railstress/VERSE/Verse%20SFT%20Measurment.jpg

Viktorov, I.A. (1966). *Rayleigh and Lamb Waves*. Plenum Press, New York.